Title

Smc5/6 association with microtubules controls dynamic pericentromeric chromatin folding

Author list

Ànnia Carré-Simon[1], Renaud Batrin[1], Sarah Isler[2], Henrik Dahl Pinholt[3], Timothy Földes[4], Guillaume Laflamme[2], Maria Barbi[4], Leonid Mirny[3,5], Damien D'Amours[2], Emmanuelle Fabre[1]*

Author affiliations

[1]Université de Paris, INSERM, CNRS, IRSL, U944, UMR7212, Paris, France

[2]Ottawa Institute of Systems Biology, Department of Cellular and Molecular Medicine, Ottawa, Canada

[3]Department of Physics, Massachusetts Institute of Technology, Cambridge, MA, USA.

[4] Sorbonne Université, CNRS, LPTMC, Paris, France

[5]Institute for Medical Engineering and Science, Massachusetts Institute of Technology, Cambridge, MA, USA

Contact information

*Correspondance : emmanuelle-g.fabre@inserm.fr

Abstract

Centromeres and pericentromeres are specialized chromatin regions whose organization is critical for proper chromosome segregation through dynamic microtubule attachment. Smc5/6, highly enriched in pericentromeres, associates with microtubules. However, whether Smc5/6 contributes to chromatin folding and dynamics in these regions remains unclear. Here, we dissect Smc5/6 function at budding yeast centromeres by constructing *smc5-2KE,* a separation-of-function mutant that reduces microtubule binding by replacing two lysines (K624 and K631) at the Smc5 hinge with glutamic acid. After demonstrating reduced microtubule binding by *smc5-2KE in vitro*, we use high temporal resolution imaging in living cells and polymer modeling to show that Smc5/6 and microtubule binding restricts chromatin dynamics along chromosome arms, thus contributing to pericentromeric chromatin folding. The *smc5-2KE* mutant shows a strong pericentromere-specific reduction in homologous recombination repair, as well as defects in mitotic spindle length, centromere clustering and cytokinesis. Overall, our results reveal that Smc5/6-microtubule association ensures robust pericentromeric chromatin folding, contributing to genome integrity in the face of mitotic forces.

Key words

Smc5/6, microtubules, pericentromeres, DNA double-strand break repair, chromatin dynamics.

41 ## Introduction

42 The three-dimensional architecture of the genome governs gene expression, DNA replication
43 and repair [1]. Centromeres are specialized regions within this chromosomal architecture that
44 serve as scaffolds for microtubule attachment via the kinetochore, a complex of around 80
45 proteins [2,3]. Surrounding the centromere, pericentromeric regions adopt a distinct chromatin
46 configuration that is essential for genome stability [4]. Pericentromeric configuration and
47 centromere/kinetochore assembly are crucial to counterbalance the mechanical forces
48 exerted by spindle microtubules during mitosis. Yet, how pericentromeric structure is shaped
49 to resist the forces exerted by microtubules is poorly understood [5,6]. In budding yeast,
50 pericentromeres span around 30-50 kb [7] and are highly enriched in structural chromosome
51 maintenance (SMC) complexes, which include cohesins, condensins and the Smc5/6 complex
52 (Smc5/6 in short) [8–11]. Cohesins and condensins participate in the establishment of DNA loops
53 that resist mitotic spindle forces [12]. While assembly of an Smc5/6 dimer was recently shown
54 to contribute to chromatin loop folding[13], the folding function of Smc5/6 at pericentromeres
55 is unknown.

56 Smc5/6 is composed of Smc5, Smc6 and non-SMC proteins (Nse1, Mms21 and Nse3-6) [14].
57 Smc5 and Smc6 consist of antiparallel coiled-coil arms that dimerize via a hinge domain at one
58 end and are linked at the other end by their ATPase head domains. As a key player in genome
59 stability that mediates post-translational modifications (PTMs), Smc5/6 interacts with many
60 chromosome proteins during the course of its cellular functions [14]. One of the most intriguing
61 interactors of the complex is the alpha/beta tubulin dimer. We previously showed *in vitro* that
62 the hinge domain of the Smc5 protein binds the tubulin dimer exclusively in the form of
63 microtubule polymers. The hinge domain contains three lysines (K624, K631 and K667) that
64 interact directly with the C-terminal negatively charged tails of tubulins [15]. Two of these
65 lysines (K624 and K631) lie in a specific C domain loop unique to Smc5/6, according to X-ray
66 crystal structures of the *S. pombe* Smc5 hinge domain [16].

67 In addition to its role in maintaining telomeres and rDNA organization [17–19], Smc5/6 also
68 participates in genome integrity by promoting the repair of damaged DNA [14,20]. Smc5/6 is
69 recruited within ~5kb of double strand breaks (DSB) [21,22], holds the DSB ends together [23] and

70 facilitates homologous recombination (HR) [18,24–26], a DNA repair process that uses a
71 homologous sequence as a template to accurately repair DSBs [27].

72 Here, we examine the role that the association between Smc5/6 and microtubules plays in
73 pericentromeric chromatin folding. We combine mutational analysis and fluorescence
74 microscopy in living cells with polymer simulations to show that the association between
75 microtubules and Smc5/6 impacts pericentromeric chromatin folding and integrity.

76 Results

77 The *smc5-2KE* mutant leads to increased chromatin dynamics at centromeres and beyond

78 To investigate the impact of the association between microtubules and Smc5/6 on chromatin
79 folding and dynamics, we modified the electrostatic charge-dependent attraction between
80 the C-terminal tubulin tails of microtubules and the Smc5 hinge [15]. We mutated K624 and
81 K631 to negatively charged glutamic acid residues resulting in the *smc5-2KE* mutant. The
82 microtubule-binding capacity of the *smc5-2KE* mutant was assessed *in vitro* by comparing the
83 co-sedimentation of purified Smc5 and Smc5-2KE proteins with microtubules. We observed a
84 3-fold reduction in the binding affinity of Smc5-2KE compared to wild-type (WT) Smc5 (**Fig.
85 1a, Fig. S1a**). The reduced affinity of Smc5-2KE for microtubules was not due to a defect in
86 the mutant's interaction with other proteins in the Smc5/6 complex, as indicated by co-
87 immunoprecipitation (CoIP) of the Nse3 subunit with both WT Smc5 and the Smc5-2KE (**Fig.
88 1b**). The preservation of Smc5/6 function in the *smc5-2KE* mutant is consistent with the
89 absence of significant defects in cell growth, cell division or cell cycle progression in mutated
90 cells (**Fig. S1b-d**). Therefore, we used *smc5-2KE* as a separation-of-function mutant that is
91 specifically defective in microtubule binding, to explore the role of Smc5/6 association to
92 microtubules in chromatin dynamics *in vivo*.

93 We first assessed chromatin dynamics as a function of nuclear localization in different cellular
94 conditions in both WT and *smc5-2KE* mutant. We tracked a GFP-labelled chromatin array
95 (tetO-TetR-GFP) positioned at 11, 90, and 730 kb from centromere IV (CEN IV) and calculated
96 the mean square displacement (MSD) as previously described [28,29] (Methods). In WT cells, the
97 different tracked loci followed a sub-diffusive movement characterized by an anomalous

98 α exponent below 1.0 (between 0.59 and 0.61, **Fig. 1c, Fig. S2a**). These values of α, typical of
99 self-avoiding bead-spring polymer models [30], indicate that the connectivity of the
100 chromosome, qualitatively determining the nature of its dynamics, is independent of its
101 distance from the centromere. However, the sub-diffusive coefficient D, as well as MSD at 10s
102 (MSD_{10s}), indicated higher mobility at positions further from the CEN IV centromeric
103 attachment point, as previously documented (**Fig. 1c-d, Fig. S2a**) [29,31–34]. Interestingly, sub-
104 diffusive chromatin motion was maintained in *smc5-2KE* mutated cells with a similar α
105 parameter, but an increase in chromatin dynamics, characterized by an increase in D, was
106 observed at all loci compared to WT cells. The increase in chromatin dynamics in mutated
107 cells was more pronounced the closer the locus was to the centromere (**Fig. 1c-d**). MSD_{10s}
108 increased in the *smc5-2KE* mutant by factors of 1.36, 1.18 and 1.07 for distance 11, 90 and
109 730 kb from CEN IV, respectively (**Fig. S2b**). Increased chromatin mobility of the *smc5-2KE*
110 mutant was verified for another locus located at 90 kb from CEN V (**Fig. S2c**) and observed at
111 different phases of the cell cycle, including G1 and metaphase (**Fig. S3**).

112 Lysine residues undergo a wide range of reversible PTMs such as SUMOylation, acetylation
113 and ubiquitination, which can regulate protein functions, including protein-protein
114 interactions [35]. To determine whether lysine PTMs are involved in the Smc5 effect on
115 chromatin mobility, we mutated both lysines to arginine (a positively charged amino acid
116 unaffected by PTM). This *smc5-2KR* mutant showed chromatin mobility like WT (**Fig. S2c**).
117 Conversely, we show that the effects of Smc5 on chromatin mobility are due to the positive
118 charge of the lysines, as the *smc5-2KA* mutant, where lysines are mutated to alanine (a neutral
119 amino acid), increased chromatin mobility like the *smc5-2KE* mutant (**Fig. S2c**). We conclude
120 that it is the presence of positive charges at amino-acid positions 624 and 631 of Smc5, rather
121 than their potential to be modified by PTMs, that is required to promote normal chromatin
122 dynamics *in vivo*.

123 Altogether, our results support the hypothesis that lysines K624 and K631, conserved in the
124 C domain of Smc5 hinge, limit chromatin dynamics possibly by associating to microtubules
125 through their positive charge, as observed *in vitro*.

126 Increased chromatin dynamics of the *smc5-2KE* mutant is not linked to spontaneous DNA
127 damage or loss of Smc5/6

128 Increase in chromatin dynamics is part of the DNA Damage Response [36,37]. To determine
129 whether increased chromatin mobility of the *smc5-2KE* mutant results from spontaneous
130 DNA damage, we first monitored Rad52 foci, as a marker of DNA repair at sites of damage [38].
131 While treatment with the genotoxic agent Zeocin yielded a similarly high number of Rad52
132 foci in WT and *smc5-2KE* mutant (74% ± 6.7 and 79,5% ± 7.8 foci respectively), we observed
133 comparable low levels of Rad52 foci in WT and *smc5-2KE* strains in the absence of Zeocin (7%
134 ± 1.1 and 8.9% ± 1.3 foci respectively) (**Fig. S4a**). We also analyzed Rad53 phosphorylation, a
135 checkpoint modification induced by DNA damage [39]. Rad53 phosphorylation was not detected
136 in *smc5-2KE* cells in the absence of Zeocin, in contrast to Zeocin-treated WT and mutant cells
137 (**Fig. S4b**). Finally, we investigated the phosphorylation of histone H2A (γH2A), a conserved
138 PTM induced by DNA damage [40]. Upon Zeocin treatment, WT and *smc5-2KE* cells displayed
139 increased levels of γH2A, while γH2A background levels were similar in untreated strains (**Fig.**
140 **S4c**). These observations are consistent with the lack of Rad53 phosphorylation and γH2A
141 observed upon Smc5/6 complex degradation [41]. Taken together these results establish that
142 the increased chromatin dynamics observed in the *smc5-2KE* mutant are not due to higher
143 levels of spontaneous DNA damage.

144 Our results show that the K624E and K631E mutations do not affect the stability of Smc5/6 *in*
145 *vitro* (**Fig. 1b**), but we could not exclude that a defect in the complex, undetectable *in vitro*,
146 could account for the increased chromatin mobility of the *smc5-2KE* mutant *in vivo*. To
147 address this point, we investigated chromatin mobility in cells defective for Smc5/6 by
148 specifically degrading Smc5 or Smc6 proteins using the auxin-inducible degron (AID) strategy.
149 Cells expressing tagged Smc5 or Smc6 proteins grew like WT cells in the absence of auxin but
150 failed to grow in the presence of 1 mM auxin (**Fig. S5a-b**). This indicates efficient degradation
151 of the tagged proteins and confirms that complete loss of Smc5 and Smc6 proteins is
152 incompatible with cell viability, in contrast to the separation-of-function phenotype of the
153 *smc5-2KE* mutant. Degradation took place 30 minutes after auxin addition, as shown by
154 western blot for Smc5-AID (**Fig. S5c**). Surprisingly, a reduction in chromatin dynamics in the
155 pericentromeric region, at 11 kb from the centromere, was observed when Smc5-AID or
156 Smc6-AID protein degradation was induced by 1h auxin addition (**Fig. S5d-f**). These findings
157 also contrast with the increase in chromatin dynamics we observed upon degradation of the
158 Smc1 subunit of cohesin (**Fig. S5e-f**), as previously documented [34,42]. The opposite effects of

159 Smc5/6 and cohesins on chromatin mobility suggest the implication of different mechanisms,
160 which in the case of cohesins might depend on their loop extrusion activity [43,44]. Taken
161 together, these results establish that Smc5/6 is required in maintaining chromatin dynamics
162 which is itself constrained by the possible association of Smc5 with microtubules.

163 The binding of microtubules to kinetochores is necessary but not sufficient to control 164 pericentromeric chromatin dynamics

165 The constraint of pericentromeric chromatin dynamics is in line with studies in budding yeast,
166 showing that release of centromeres from their attachment to the SPB upon microtubule
167 depolymerization or centromere inactivation leads to enhanced chromatin mobility [34,45–47].
168 We therefore first investigated chromatin mobility following microtubule depolymerization
169 by nocodazole in WT and in the *smc5-2KE* mutant. We exposed cells to a short treatment (30
170 minutes) with nocodazole (**Fig. 2a**) and analyzed chromatin dynamics at different
171 chromosome locations. This treatment depolymerized microtubules, as confirmed by the
172 absence of microtubule filaments visualized by Tub2-GFP (**Fig. 2b**) but did not block cells
173 cycling (**Fig. 2c**). In WT cells, chromatin mobility increased upon exposure to nocodazole at
174 loci far from the centromere, *i.e.* at 90 kb and 730 kb from the centromere, as previously
175 observed (**Fig. 2d, 2g**) [45,46]. In contrast, in the *smc5-2KE* mutant, nocodazole had no significant
176 effect on chromatin mobility, indicating that the lack of microtubules or the Smc5-2KE
177 mutation leads to a similar increase in chromosome dynamics with no cumulative effect of
178 the two. Close to the centromere at 11kb from CEN IV, nocodazole caused a significant
179 increase in chromatin dynamics, however, to a lesser extent than that observed in the *smc5-*
180 *2KE* mutant (MSD_{10s} 1.14 vs. 1.32 respectively**, Fig. 2d**). These observations support the view
181 that binding of microtubules to Smc5/6 limits chromatin mobility throughout the
182 chromosome and that in the pericentromeric region, Smc5/6 plays an additional role, possibly
183 affecting chromatin properties.

184 We next analyzed chromatin dynamics in two kinetochore thermosensitive mutants *ndc80*-1,
185 which impairs kinetochores-microtubules binding [48] and *ndc10*-1, which affects centromeric
186 chromatin binding [49]. To effectively compare these mutants to *smc5-2KE*, we first confirmed
187 that the chromatin behavior reported in the *smc5-2KE* mutant at 30°C is also observed at
188 37°C, the restrictive temperature for these mutants. Chromatin dynamics at 90 kb from CEN

189 V displayed a comparable increase between *ndc80-1* and *smc5-2KE* single mutants at 37°C
190 (**Fig. 2e left, 2f**), with no additive effect in the *ndc80-1 smc5-2KE* double mutant (**Fig. 2e left,**
191 **2f**). Conversely, the *ndc10-1* mutant showed no increase in chromatin dynamics compared to
192 the WT, while the Smc5-2KE mutation induced an increase in chromatin mobility **Fig. 2e right,**
193 **2f**). These results indicate that only kinetochore mutations disrupting microtubule binding
194 have an impact on chromatin dynamics.

195 These data confirm that the *smc5-2KE* mutant acts as expected for a variant with reduced
196 microtubule binding. In addition, our analysis collectively demonstrates that changes in
197 microtubule binding, whether due to kinetochore mutants or microtubule depolymerization,
198 are sufficient to enhance chromatin dynamics away from the centromere.

199 ## The *smc5-2KE* mutant modifies pericentromeric chromatin properties

200 The results above suggested that *smc5-2KE* mutant may reveal an additional effect of the Smc
201 5/6 interaction: impacting chromatin properties at pericentromeres. To evaluate the impact
202 of the *smc5-2KE* mutant on these properties, we compared intra-chromosomal distances of
203 different loci in WT and mutant cells. Changes in intra-chromosomal distances underline
204 changes in compaction, rigidity or loop extrusion activity [23,29,50]. We used strains R1 and R3
205 where pairs of differently fluorescently-labelled loci, distant by ~180 kb, are scattered on
206 chromosome IV [29] (Methods). The R1 strain has one labelled locus in a pericentromeric
207 position (at 4 kb from CEN IV, **Fig. 3a**) and the R3 strain has two labelled loci located centrally
208 on the chromosome arm (at 735 kb from CEN IV, **Fig. 3b**). The *smc5-2KE* mutation was
209 introduced in both strains, and 2D distances between pairs of loci were measured from 3D
210 images (Methods). As a control, we used Zeocin, which promotes an increase in intra-
211 chromosomal distances, as previously shown (**Fig. 3a-b**) [29,50]. While intra-chromosomal
212 distances between pair of loci in R3 strain remained similar between R3 WT and R3 *smc5-2KE*
213 strains (**Fig. 3b**), a significant increase in intra-chromosomal distances was observed in the R1
214 *smc5-2KE* mutant compared to the R1 WT strain (**Fig. 3a**). This increase suggests that at this
215 sub-chromosomal scale, changes in chromatin properties occur in the *smc5-2KE* mutant,
216 which are revealed when at least one locus is pericentromeric. Although these data do not
217 precisely define whether chromatin decompaction or stiffening are induced by the *smc5-2KE*

218 mutant, they do indicate that the K624 and K631-dependent association of Smc5 with
219 microtubules is required to establish or maintain pericentromeric chromatin.

220 Polymer model recapitulates changes in chromatin dynamics at pericentromeres

221 We next used biophysical polymer simulations (Methods) to determine if in the
222 pericentromeric region, microtubule binding and chromatin structure together could drive
223 chromatin dynamics. Initially, we assessed chromatin mobility at positions corresponding to
224 11, 23, 90 and 730 kb from the centromere of different chromosomes. Polymer simulation
225 showed that the increase of MSD_{10s} was proportional to the distance to the centromere as
226 observed *in vivo* and plateaued at 90 kb (**Fig. 4a** compared to **Fig. 1c**). Although the increase
227 in mobility in the polymer model was less pronounced than in the experimental data, the
228 relative features were present and would allow investigation of the effects of perturbations.

229 We then modified variables related to microtubule tethering and chromatin stiffness and
230 analyzed simulated chromatin dynamics. We first investigated the effect of weakening
231 microtubule tethering to the kinetochore. The spring constant of the harmonic bond between
232 the centromere and the SPB was loosened from a value ensuring a fixed bond to one yielding
233 an energy of 1kbT at 105 nm extension from the 400 nm rest length. Loosening the
234 attachment increased mobility for loci 11 kb away from the centromere, as we observed when
235 microtubules were depolymerized by nocodazole, but left loci 90 kb unchanged **(Fig. 2d, Fig.
236 4b** and **Fig. S6**), indicating that tethering by microtubules induces only a local effect on
237 chromatin mobility (see discussion). We then modified chromatin state by increasing global
238 chromatin stiffness. In contrast to the position-dependent change when weakening
239 microtubule tethering, this led to a global mobility increase independent of the distance from
240 the centromere (**Fig. 4c** and **Fig. S7**). This is expected, as even in the simple Rouse model,
241 mobility increases when the spring constant between monomers increases [29].

242 We reasoned that both effects could be at play in the pericentromeric region since the Smc5-
243 2KE mutation displayed a greater increase in mobility than the nocodazole treatment. To test
244 if this was possible, we combined a stiffness increase with the loosened chromatin tethering
245 to microtubules. We observed that stiffening further increased chromatin dynamics, like the
246 results seen *in vivo* for the difference between WT nocodazole and the *smc5-2KE* mutant (**Fig.**

247 **2d, Fig. 4d and Fig. S8**). These results show that a relaxation of microtubule attachment and
248 a stiffer chromatin are sufficient to explain the increase in pericentromeric chromatin
249 dynamics observed *in vivo* in the *smc5-2KE* mutant. They further support our hypothesis that
250 Smc5 binds to both microtubules and chromatin to maintain pericentromeric chromatin
251 folding and dynamics.

252 ## The *smc5-2KE* mutant affects homologous recombination at pericentromeres

253 Chromatin organization plays a central role in the efficiency of DSB repair [51–53] and Smc5/6
254 also contributes to DSB repair via. To assess whether the *smc5-2KE* mutant influences DSB
255 repair by HR both near and far from the centromere, we used a system tracking HR upon a
256 single DSB induction [54] (**Fig. 5a**). I-*Sce*I is expressed on plasmid with the galactose-inducible
257 *GAL1-10* promoter to induce the DSB (+DSB), while an empty vector serves as control (-DSB).
258 Successful HR between donor and recipient sequences leads to mCherry expression,
259 detectable by red fluorescence in living cells (**Fig. 5a**). Recipient mCherry sequence was
260 introduced at 5 kb (named C) and 404 kb (named L) from CEN IV in both the WT and the *smc5-*
261 *2KE* mutant strains, resulting in four distinct strains (**Fig. 5b**). The I-*Sce*I cleavage efficiency in
262 these strains, quantified by qPCR, was ~80%, after 6 hours of I-*Sce*I induction, irrespective of
263 the position of the cutting site [54] (**Fig. S9a**). Cell survival was assessed by colony forming unit
264 (CFU) assays. As expected, in the absence of I-*Sce*I, WT and *smc5-2KE* C and L colonies grew
265 in both inducing and non-inducing conditions (**Fig. 5b**), while DSB induction by I-*Sce*I led to a
266 severe growth defect in the absence of the donor, in all four strains, with a CFU of almost 0%
267 (**Fig. 5b**).

268 Interestingly, providing the donor sequence on the dCEN plasmid to allow DSB repair by HR,
269 had different outcomes in *smc5-2KE* depending on the DSB position. When the DSB was in
270 the pericentromeric region, the *smc5-2KE* mutant showed significantly reduced survival rates
271 compared to the WT (C strains, 15 ± 6% and 55 ± 12.4%, respectively, **Fig. 5b**). In contrast,
272 both WT and the *smc5-2KE* mutant presented similar survival rates for a DSB located in the L
273 position (40 ± 7.5% for both L strains) (**Fig. 5b**). Importantly CFU values and the percentage of
274 mCherry-expressing cells were consistent across conditions, confirming that survival was due
275 to successful HR. At the C position, 44 ± 3.4% of WT cells and only 22.5 ± 1.7% of *smc5-2KE*
276 cells expressed mCherry (**Fig. 5c**). However, at the L position, both WT and *smc5-2KE* strains

277 showed similar mCherry expression levels (36 ± 2.5% for both; **Fig. 5c**). HR defect could not
278 be explained by a change in Smc5/6 occupancy at DSB, as ChIP-qPCR of Smc5-MYC or *smc5-*
279 *2KE*-MYC revealed no significant differences, irrespective of the DSB position (**Fig. S9b-c**).
280 Taken together, these results demonstrate that Smc5/6 is required for HR at the
281 pericentromeres, but not along the chromosome arm, and reveal the role for Smc5 binding
282 to microtubules in pericentromeric integrity.

283 Local mobility induced by a DSB is facilitated by microtubules and has been proposed to
284 promote DSB repair by HR [45,55]. We therefore analyzed chromatin mobility at the DSB in the
285 *smc5-2KE* mutant. We introduced a lacO-LacI-GFP array at 10 kb away from the I-*Sce*I cutting
286 site in WT and mutant C and L strains and verified by qPCR that the efficiency of I-*Sce*I cutting
287 was not affected by the array in all strains (80% at 6 hours after induction) (**Fig. S9d**).
288 Chromatin dynamics was tracked after 6 hours of induction, and MSD was plotted through
289 increasing time intervals (**Fig. 5d**, **Fig. S9e**). DSB induction in WT led to an increase in
290 chromatin dynamics, independently of the DSB position, whereas in the *smc5-2KE* mutant,
291 DNA damage did not cause an additional increase in mobility on top of the one generated by
292 the mutation, as reported above (**Fig. 1**, **Fig. 5d**, **Fig. S9e**). These results show that differences
293 in HR efficiency between a pericentromeric DSB and a mid-arm DSB are not related to changes
294 in local chromatin dynamics and suggest that smc5-microtubule association is required for a
295 fraction of the mobility induced by a DSB.

296 The *smc5-2KE* mutant alters the mitotic spindle integrity

297 A correlation between pericentromeric chromatin compaction and spindle elongation has
298 been reported previously [6,56]. Since our results point to a role of the association between the
299 Smc5/6 and microtubules on the dynamics and properties of pericentromeric chromatin, this
300 suggests that Smc5/6 may also regulate the mitotic spindle. To explore this hypothesis, we
301 first studied spindle length by measuring the distance between each spindle pole body in
302 dividing cells. We used SPB protein Spc42 fused to mCherry [57] to calculate the 2D distances
303 between the two fluorescent centers of mass as above (**Fig. 3, Fig. 6a left**). In WT cells, spindle
304 length average was 1.18 ± 0.29 µm, whereas *smc5-2KE* mutant exhibited a significant increase
305 to 1.32 ± 0.33 µm (p value < 0,0001) (**Fig. 6a left**), suggesting that the binding between Smc5
306 and microtubules contributes to the regulation of the spindle length.

307 Alterations in spindle length can arise from changes in the length of the kinetochore
308 microtubules connecting centromeres to the SPB, or modifications in the
309 kinetochore/pericentromere itself. Measuring the distance between GFP-tagged CEN IV and
310 Spc42-mCherry showed no difference between the WT and *smc5-2KE* mutant (**Fig. 6a right**).
311 As a control, Zeocin increased CEN-SPB distance as already demonstrated (**Fig. 6a right**) [29,50],
312 suggesting that *smc5-2KE* does not alter the kinetochore microtubules length. To evaluate the
313 kinetochore integrity in the *smc5-2KE* mutant, we measured centromere clustering *in vivo* by
314 visualizing kinetochore protein Mtw1 fused to 3xGFP at the endogenous locus [47]. Mtw1 is a
315 kinetochore-specific protein, part of the MIND complex, which links the inner and outer layers
316 of the kinetochore [58]. While Mtw1-3xGFP expressing cells cycled normally, combination with
317 *smc5-2KE* surprisingly led to a mitosis defect reminiscent of the no-cut phenotype, where
318 completion of cytokinesis is delayed [59]. This suggests that Mtw1-3xGFP fusion constitutes a
319 hypomorphic allele, leading to a kinetochore and mitotic spindle length defect detectable in
320 the presence of *smc5-2KE*.

321 In WT cells, Mtw1-3xGFP formed a single fluorescent focus due to the centromeric clustering
322 typical of the Rabl configuration. Treatment with the microtubule-depolymerizing drug
323 nocodazole induced fragmentation of the Mtw1-3xGFP labelling into several foci, consistent
324 with centromeres declustering, as previously reported [60]. Strikingly, the *smc5-2KE* mutant
325 presented a high percentage of cells with centromere declustering compared to WT (27.26 ±
326 4.3% and 9.89 ± 2.5% for *smc5-2KE* and WT cells respectively, **Fig. 6c**).

327 Altogether, our results show that *smc5-2KE* mutant has defects in spindle length and, in
328 combination with Mtw1-3xGFP, in cytokinesis and centromere clustering. Furthermore, these
329 results suggest that the association between Smc5/6 and microtubules ensures that
330 pericentromere structure forms robustly.

331 Discussion

332 Pericentromeres across eukaryotic evolution are enriched with SMC complexes, which share
333 the conserved role of extruding DNA to create loops [13,61,62]. The pericentromeric enrichment of
334 SMCs and their extruding activity theoretically leads to a structure described, from a physical
335 perspective, as a bottlebrush, balancing the outward pulling forces of microtubule with the

336 inward attractive forces of chromatin during cell division [4]. Smc5/6 has been shown to associate
337 with microtubules in budding yeast and *Xenopus* [15,63]. However, the role of this association in
338 organizing pericentromeric structure *in vivo* was previously unknown. By measuring chromatin
339 dynamics in the *smc5-2KE* mutant, which decreases the affinity between Smc5 and
340 microtubules, we demonstrate that Smc5 associates with microtubules *in vivo* and regulates
341 chromatin mobility along the chromosome, as well as chromatin properties in the
342 pericentromeric region. Moreover, we show that Smc5/6 association with microtubules
343 specifically contributes to DSB repair efficiency in the pericentromeric region and maintains the
344 integrity of the mitotic spindle.

345 We provide evidence that the conserved residues K624 and K631 in the hinge region of Smc5
346 connect the protein to microtubules both *in vitro* and *in vivo.* First, the *smc5-2KE* mutant shows
347 a decrease in microtubule binding by co-sedimentation assay (**Fig. 1a**). Second, in this mutant,
348 chromatin dynamics far from centromeres mirror microtubule depolymerization (**Fig. 2d, 2f**)
349 and resemble the effects observed in the *ndc80-1* kinetochore mutant (**Fig. 2e-f**). Third,
350 combining *smc5-2KE* with *ndc80-1* or with microtubule depolymerization by nocodazole shows
351 no additional effects on chromatin dynamics. This supports the idea that the association of
352 Smc5 with microtubules specifically requires both residues K624 and K631, only. Fourth,
353 polymer modelling shows that loosening the interaction between centromeres and the SPB
354 increases pericentromeric chromatin mobility, as observed in the *smc5-2KE* mutant (**Fig. 4b,**
355 **4d**). Finally, the *smc5-2KE* mutant affects the mitotic spindle, including spindle length (**Fig. 6a**),
356 and when combined with the kinetochore protein Mtw1-3xGFP, centromere clustering and
357 cytokinesis (**Fig. 6b-c**). The ability of Smc5/6 to bind microtubules, regardless of the phase of
358 the cell cycle, is thus an important emerging property of this complex.

359 The association between Smc5/6 and microtubules has critical consequences for the folding
360 of the pericentromeric region. In this region, measurements of both chromatin mobility and
361 intra-chromosomal distances in the *smc5-2KE* mutant indicate that reduced association with
362 microtubules, and only them, impacts chromatin structure, potentially leading to increased
363 rigidity or decompaction, as shown by polymer modelling. How could the Smc5-2KE mutation
364 affect the properties of pericentromeric chromatin? Loss of microtubules polymerization or
365 Ndc80 kinetochore mutants, such as Gal-Nuf2, where Nuf2 is repressed in the presence of

366 glucose, result in decreased levels of histone H4 and H2B in the pericentromere, as shown by
367 FRAP [64]. The fact that a reduction of histones has been related to chromatin decompaction
368 together with increased chromatin dynamics [42,45,50], suggests that disruption of microtubule-
369 induced tension in the *smc5-2KE* mutant could result in decreased levels of histones in the
370 pericentromeric region, chromatin decompaction and subsequent chromatin mobility
371 increase. Moreover, loss of microtubules polymerization increases intra-chromosomal
372 contacts and affects pericentromeric configuration [7], suggesting that the tension created by
373 microtubules can regulate chromatin structure close to microtubules attachment [7].
374 Therefore, the interaction between Smc5 and microtubules, disrupted in the *smc5-2KE*
375 mutant, might regulate the microtubule-induced tension that influences pericentromeric
376 chromatin folding.

377 Another interesting possibility is that the Smc5/6 complex regulates pericentromeric
378 chromatin structure via its DNA compaction activity, consistent with recent single molecule
379 experiments [65,66]. Mechanistically, we cannot exclude that the modification of the
380 pericentromeric chromatin structure in the *smc5-2KE* mutant could be related to the loop
381 extrusion capacity of Smc5/6 dimers, as recently demonstrated [13]. If mutation of both K621
382 and K634 alters dimerization or stabilization of the two Smc5/6 complexes, it could disrupt
383 loop extrusion, impacting persistence length and/or chromatin compaction. However,
384 depletion of the entire complex, which consequently abolishes loop extrusion activity, has an
385 impact on chromatin mobility opposite to the Smc5-2KE mutation, suggesting distinct roles
386 on chromatin properties (**Fig. S5d**). Alternatively, cohesin or condensin recruitment could be
387 compromised in the *smc5-2KE* mutant leading to decompaction/stiffening, at the chromatin
388 scale, of the pericentromeric region [5] and, subsequently, increased chromatin dynamics (**Fig.
389 1c**) [34,42,67].

390 It is intriguing that disrupting the microtubule binding to centromeres, either by
391 depolymerization of microtubules in the presence of nocodazole, by affecting the kinetochore
392 in the *ndc80-1* mutant or with the *smc5-2KE* mutant results in increased chromatin dynamics
393 not only close to the centromere but also at locations distant from it. It is possible that once
394 centromeres are freed from microtubules, they exhibit increased movement, which could be
395 translated into greater chromatin mobility further along the chromosome. By analogy, a rope

396 with movement at one end could lead to increased movement at the other end. However, by
397 simulating weakened microtubule anchoring, the polymer model fails to fully reproduce the
398 *in vivo* increase in chromatin dynamics away from the centromere (**Fig. 4b**), possibly due to
399 unmodeled features such as SMC-mediated loop formation or centromeres declustering,
400 which might influence chromatin density *in vivo.*

401 One of the pericentromeric chromatin functions mediated by the association of the Smc5/6
402 complex with microtubules is clarified by the "no-cut" phenotype (**Fig. 6b**). Defects in
403 cytokinesis are indeed observed when the *smc5-2KE* mutant is combined with Mtw1-3xGFP.
404 This phenotype, also described in cells with mutations in kinetochore proteins such as *ndc10-*
405 *1* and *ndc80-1* alleles [59,68] suggests that the interaction between the Smc5-2KE mutation and
406 Mtw1-3xGFP is associated with compromised kinetochores [69]. Interestingly, the “no-cut”
407 phenotype has been described in cells with incomplete DNA segregation [70], indicating that
408 disruption in chromosome segregation can lead to cytokinesis defects. Thus, it is conceivable
409 that the combination of Smc5-2KE with Mtw1-3xGFP results in chromosome segregation
410 defects leading to the “no-cut” phenotype and pinpoints to the important function of Smc5/6
411 in establishing pericentromeric chromatin through its association with microtubules.

412 It has previously been shown both in budding yeast and mammalian cells, that Smc5/6 is
413 enriched around DSBs [21,22,71] and contributes to HR by resolving Holliday junctions [18,25,26], as
414 well as by maintaining the ends of a DSB together [23]. In line with the role of Smc5/6 in HR, we
415 show that the Smc5-2KE mutation leads to reduced repair efficiency only at pericentromeres
416 (**Fig. 5**). In this chromatin context, the lack of association between Smc5/6 and microtubules
417 may indirectly impact HR efficiency through microtubule-induced chromatin properties
418 perturbations that we reported in this region (**Fig. 3**). Yet, the *smc5-2KE* mutant could also
419 directly impair pericentromeric DSB repair. First, mutating the hinge domain of Smc5, which
420 has been shown to have affinity for ssDNA *in vitro* [16,72], could affect the putative interaction
421 between the Smc5/6 complex and ssDNA at DSB, potentially impacting 5’ DNA resection at
422 DSBs or the maintenance of the DSB ends [23]. Second, the lack of association between
423 microtubules and the Smc5/6 could hinder the efficient relocalization of damaged
424 pericentromeres to the nuclear periphery, in line with the reported role of the Smc5/6
425 complex relocalization for DSBs in repetitive rDNA sequences in budding yeast [73] and in

426 heterochromatin in *Drosophila* [74,75]. Third, upon a DSB near the centromere, DNA resection
427 may lead to detachment of the centromere from microtubules, triggering the formation of
428 damage-induced microtubules (DIM) to recapture the centromere as proposed [76]. This
429 process would require Smc5/6; thus, a mutation affecting association with DIMs could
430 hamper centromere recapture and efficient DSB repair.

431 Taken together, our focus on chromatin dynamics emerged as a powerful approach for
432 understanding the functional relevance of the association between Smc5/6 with microtubules
433 on the maintenance and integrity of pericentromeric chromatin. We propose that the
434 enrichment of Smc5/6 at pericentromeres, together with its association with microtubules,
435 contribute to the maintenance of pericentromere chromatin stability in the face of mitotic
436 forces. Smc5/6 enrichment in the pericentromeric region is conserved throughout mitosis of
437 many organisms [9,22,77]. It is likely that a similar association between Smc5/6 and microtubules
438 occurs in mammals during open mitosis, the only phase when microtubules interact with
439 centromeric regions in mammals. Therefore, the role of Smc5/6 in preserving pericentromeric
440 structure during mitosis might be conserved through evolution.

441 Acknowledgements

442 We thank A. Marston, P. Hieter and T. Teixeira for sharing strains and plasmids. We also thank
443 E. di Santo and C. Marquez for their participation in strains constructions. Our
444 acknowledgements go to X. Zhao for enlightening discussions, P. Lesage, F. Garcia-Fernandez
445 and S. Mihic for their constructive reading of the manuscript. P. Therizols and the members
446 of the laboratory are thanked for the many lively discussions on this project and the GDR
447 Architecture Dynamique du noyau et des génomes (ADN&G) for the valuable exchanges with
448 its community. This work was supported by an FRM grant to EF (EQU202203014635) and CIHR
449 grant to DD (FDN–167265). EF is also supported by PLBIO-INCA (PLBIO20-31) and DD by a
450 Canada Research Chair in Chromatin Dynamics & Genome Architecture (CRC-2017-00064).
451 ACS was supported by FRM (ECO202006011576) and ARC (ARCDOC42023010006078)
452 fellowships.

453 Legends to the figures

454 **Figure 1: The *smc5-2KE* mutant leads to an increased chromatin dynamics at centromeres**
455 **and beyond. (a)** The fraction of microtubule-bound Smc5 and Smc5-2KE from 3 independent
456 experiments was plotted as a function of microtubules (MT) concentrations. Dissociation
457 constants (Kd) were determined by curve fitting to a hyperbola. **(b)** Co-immunoprecipitation
458 (co-IP) experiments showing the association of Nse3-3xSTII with Smc5 or Smc5-2KE proteins
459 (both tagged with C-terminal 13xMYC epitopes) in yeast extracts. A whole cell extract was
460 loaded as an input (7%; **left**) and Smc5/6 complex components were immunoprecipitated
461 from this extract using StrepTactin XT® resin (**right**). For each panel, the first lane represents
462 a negative control where only Nse3 was tagged (with 3xSTII), whereas the second and third
463 lanes show Nse3-3xSTII co-purified with Smc5-13xMYC and Smc5-2KE-13xMYC proteins,
464 respectively. **(c)** Mean square displacement (MSDs) as a function of increasing time intervals
465 in the WT (blue) and in the *smc5*-2KE mutant (green) for a locus at different positions of
466 chromosome IV (11kb, 90 kb and 730 kb, from left to right). Wilcoxon rank-sum test results
467 between distributions, with the p-value. * ($p<0.05$), *** ($p<0.0001$). **(d)** Distributions of the
468 exponent alpha (upper line) and of the sub-diffusion coefficient D (lower line) for the WT
469 (blue) and in the *smc5-2KE* mutant (green) for loci at different positions of chromosome IV.
470 The values of parameters alpha and D are calculated from single trajectories as described in
471 Material and Methods. Vertical lines correspond to average values (WT in blue, *smc5-2KE*
472 mutant in green).

473 **Figure 2: The binding of microtubules to kinetochore is necessary but not sufficient to**
474 **control pericentromeric chromatin dynamics. (a)** Experimental protocol used to
475 depolymerize microtubules with 20 ng/µl of nocodazole while continued cycling. **(b)** Tub2-
476 GFP in the WT and in the *smc5-2KE* mutant with or without addition of nocodazole. **(c)** Cells
477 synchronization monitored by flow cytometry in cells treated with nocodazole (15 ng/µl).
478 Samples were taken at 0, 30 and 120 minutes after induction. **(d)** MSD as a function of
479 increasing time intervals in the WT and *smc5*-2KE mutant at 11, 90 and 730 kb with or without
480 the presence of nocodazole. Wilcoxon rank-sum test results between distributions, with the
481 p-value "ns" non-significant, *** ($p<0.0001$). **(e)** MSDs as a function of increasing time
482 intervals of the locus at 90 kb in the *ndc80-1* mutant (**left**) and *ndc10-1* mutant (**right**) with or
483 without the Smc5-2KE mutation at 37°C. Wilcoxon rank-sum test results between
484 distributions, with the p-value "ns" non-significant, *** ($p<0.0001$) **(f)** Table summarizing the

485 different conditions with values extracted from the MSD: MSD at 10 s, the anomalous
486 exponent (alpha), the sub-diffusive coefficient (D) and the number of cells analyzed.

487 **Figure 3: The *smc5-2KE* mutant changes chromatin properties in the pericentromeric region.**
488 **(a-b)** Cumulative distribution functions (CDF) show the intrachromosomal distances
489 distribution measured for two pairs of loci 180 kb apart at two different positions of the
490 chromosome IV, **(a)** close to the centromere (R1) and **(b)** in the middle of the arm (R3) **(right)**
491 in the presence or absence of Zeocin. Three experiments were done in each case: R1:
492 N_{WT}=21806, N_{2KE}=9014, $N_{WT\ ZEO}$=4091, $N_{2KE\ ZEO}$=1570 and for R3: N_{WT}=2778, N_{2KE}=4403.

493 **Figure 4:** Polymer model recapitulates changes in chromatin dynamics at centromeres: **(a)**
494 Comparison of MSDs for loci with various distances to the centromere. **(b)** Effect of increasing
495 the flexibility of the SPB tether from rigid (red curves) to a spring constant of 1kbT/ $(105\ nm)^2$
496 which would allow for a standard deviation of 74 nm (105 nm/sqrt(2)) if no other forces were
497 applied (blue curves). Left plot shows loci 11kb from the centromere and the right shows loci
498 90 kb from the centromere. Only loci on chromosomes larger than 400 kb excluding Chr XII
499 were included. The inset shows a 2D slice of the centromere positions for the loose (blue) and
500 rigid (red) centromeres. Bonds are shown in grey and scale bar is 500 nm. **(c)** Effect of
501 increasing polymer stiffness from one leading to a persistence length of 70 nm (red curves) to
502 one with an angular spring constant that is 20% higher (blue curves). Loci are as in (b). Inset
503 shows a 2D conformation of Chr I in the two conditions, scale bar is 500 nm. **(d)** MSD for loci
504 11 kb away from the centromere when comparing effects of increasing flexibility (blue and
505 red curves, same as left panel of (b)) and combining flexibility and stiffness (grey curve).

506 **Figure 5: The *smc5-2KE* mutant decreases homologous recombination efficiency at**
507 **pericentromeres. (a)** Schematic representation of the system to track homologous
508 recombination (HR). In the recipient mCherry, I-*Sce*I has a 30 bp I-*Sce*I cutting site sequence
509 followed by a stop codon (red bar) inserted at 57 amino acids from the end of
510 the mCherry coding sequence. The donor (dCen) is a full-length mCherry lacking promoter
511 and terminator sequences, carried on a centromeric plasmid. A functional mCherry could be
512 expressed only after successful HR. **(b)** Colony formation unit (CFU) test showing three
513 conditions: without DSB (-DSB), with a DSB (+DSB) and with a DSB and a donor (DSB+donor)
514 in the C and in the L strain for the WT and for the *smc5-2KE* mutant. Ratio between Induced

515 I-*Sce*I/Non induced I-*Sce*I. Three experiments were conducted with the number of cells
516 counted as follows: For the C strain, $N_{WT\ PRS}$ =487, $N_{WT\ PB}$ =528, $N_{WT\ Cen}$ =668, $N_{2KE\ PRS}$ =330, $N_{2KE\ PB}$ =620, $N_{2KE\ Cen}$ =752. For the L strain, $N_{WT\ PRS}$ =344, $N_{WT\ PB}$ =309, $N_{WT\ Cen}$ =328, $N_{2KE\ PRS}$ = 261,
518 $N_{2KE\ PB}$ =379, $N_{2KE\ Cen}$ =387. T-test was used to analyse differences between groups, with "ns"
519 for not significant (P>0.05) and ** for P<0.001. **(c)** Number of red cells (%) without DSB (-DSB),
520 with a DSB (+DSB) and with a DSB and a donor (DSB+donor) in the C and in the L strain. Three
521 experiments were conducted, counting the number of cells for the C strain as follows: $N_{WT\ PRS}$
522 =506, $N_{WT\ PB}$ =607, $N_{WT\ Cen}$ =1299, $N_{2KE\ PRS}$ = 744, $N_{2KE\ PB}$ =712, $N_{2KE\ Cen}$ =1551. For the L strain,
523 the counts were $N_{WT\ PRS}$ =962, $N_{WT\ PB}$ =799, $N_{WT\ Cen}$ =1828, $N_{2KE\ PRS}$ =943, $N_{2KE\ PB}$ =774, $N_{2KE\ Cen}$
524 =924. **(d)** MSD as a function of increasing time intervals in the WT and *smc5*-2KE mutant after
525 inducing a single DSB either at position C or L. Wilcoxon rank-sum test results between
526 distributions, with the p-value "ns" non-significant, *** (p<0.0001).

527 **Figure 6: The *smc5-2KE* mutant alters the mitotic spindle integrity. (a)** CEN IV was tagged
528 with GFP and SPB with Spc42-mCherry. 2D distances between two SPBs (red dots) (**left**) and
529 between Cen (green) and SPB (red) in dividing cells (**right**) were measured. Three experiments
530 were conducted, measuring the number of cells for SPB-SPB (N_{WT}=224, N_{2KE}=332) and for CEN-
531 SPB (N_{WT}=247, N_{2KE}=380). CEN-SPB was also measure with the presence of Zeocin with $N_{WT\ ZEO}$=1299, $N_{2KE\ ZEO}$=2033. T-test was used to analyze differences between groups, with "ns" for
533 not significant, * for (P<0.05) and *** for P<0.0001. **(b)** Mtw1-3xGFP and Smc5-2KE Mtw1-
534 3xGFP cells were counted according to their distribution in G1, S or G2/M cell cycle phases.
535 Dead cells or cells presenting defective mitosis (DF) were also counted. Three experiments
536 were conducted, counting the number of cells as follows: N_{WT}=439, $N_{WT\ NOC}$=588, N_{2KE}=413,
537 $N_{2KE\ NOC}$=652. T-test was used to analyze with * for P<0.01 and ** for P<0.001. **(c)** Mtw1 was
538 labelled with 3xGFP to measure kinetochore clusters with or without nocodazole addition (15
539 ng/µl) or without % of non-clustered cells was plotted. T-test was used to analyze differences
540 between groups, with "ns" for not significant, ** for (P<0.001).

541 **Figure S1: Smc5-2KE mutation does not affect cell growth nor cell cycle. (a)** Microtubule
542 polymer binding assay. Coomassie blue-stained gels showing the binding of the hinge region
543 of Smc5 (residues 215–885) to the microtubule (MT, µM) polymer fraction (pellet; P) after
544 centrifugation. Note how Smc5 hinge domain progressively transferred from the

545 depolymerized tubulin fraction (supernatant; S) to the polymer fraction (P) as the MT
546 concentration increased and eventually bound all available Smc5 protein (top gel). In contrast,
547 the Smc5-2KE mutant (lower gel) showed strongly reduced affinity for MT polymers, as
548 evidenced by the substantial fraction of the hinge domain remaining in the supernatant
549 fraction at the highest concentration of MT shown in the gel (4 µM). **(b)** Experimental protocol
550 used to synchronize cells in G1 using alpha factor. **(c)** Percentage of budded and late anaphase
551 cells at each time point, respectively. **(d)** Cell synchronization monitored by flow cytometry.
552 **(e)** Images showing examples of G1 (**top**), metaphase (**middle**) and anaphase (**bottom**) cell
553 morphologies monitored in yeast cultures expressing Smc5 o*r* smc5-2KE. Prior to imaging,
554 cells were fixed, washed and stained with DAPI to enable nuclei visualization. Scale bars
555 represent 5µm.

556 **Figure S2: Smc5-2KE mutation increases chromatin mobility along the arm affecting the**
557 **positive charges of K624 and K631. (a)** Table summarizing the different conditions with values
558 extracted from the MSD: MSD at 10 s, the anomalous exponent (alpha), the sub-diffusive
559 coefficient (D) and the number of cells analyzed. **(b)** Ratio of MSD at 10 s between *smc5-2KE*
560 versus WT at different positions of the chromosome IV. **(c)** MSDs as function of time in the
561 WT, *smc5-2KR* and *smc5-2KA* mutants. Wilcoxon rank-sum test results between distributions,
562 with the p-value. ns ($p>0.05$) and *** ($p<0.0001$).

563 **Figure S3. Smc5-2KE mutation increases chromatin mobility throughout the cell cycle. (a)**
564 Experimental protocol used to synchronize cells in G1 with 50 ng/ml of alpha factor (**left**). WT
565 and *smc5*-2KE MSDs at 11 and 90 Kb at G1. Wilcoxon rank-sum test results between
566 distributions, with the p-value *** ($p<0.0001$) (**right**). **(b)** Experimental protocol used to
567 synchronize in G2/M cells carrying the P_{MET3}-*CDC20* with 2 mM of methionine (**left**). WT and
568 *smc5-2KE* MSDs at 11 and 23 Kb at G2/M. Wilcoxon rank-sum test results between
569 distributions, with the p-value *** ($p<0.0001$) (**right**). **(e)** Table summarizing the different
570 conditions with values extracted from the MSD: MSD at 10 sec, the alpha, the sub-diffusive
571 coefficient (D) and the number of cells analyzed.

572 **Figure S4. The *smc5-2KE* mutant does not induce spontaneous DNA damage. (a)** Rad52-foci
573 (protein involved in HR) in WT and *smc5-2KE* mutant (2KE). Three experiments were
574 conducted with the number of cells counted as follows: N_{WT}=608, N_{2KE}=1388, $N_{WT\ ZEO}$=650,

575 $N_{2KE\ ZEO}$=509. T-test was used to analyze differences between groups, with "ns" for not
576 significant and *** for P<0.0001. **(b)** Representative results from immunoblotting showing
577 the phosphorylation (Ph) status of Rad53 in WT, *smc5-2KE* cells and in response to Zeocin
578 treatment (zeo). Actin was used as a loading control. Blots are representative of three
579 experiments. **(c)** Representative results from immunoblotting showing the phosphorylation
580 of H2A (γH2A) in WT, *smc5-2KE* cells and in response to Zeocin treatment. Actin was used as
581 a loading control. Blots are representative of three experiments (**left**). Protein levels are
582 represented as mean ratio values quantified from protein γH2A versus. Actin compared to the
583 WT (**right**).

584 **Figure S5. The Smc5 or Smc6 degradation decreases chromatin dynamics. (a)** Experimental
585 protocol used to synchronize cells in metaphase with 2 mM of methionine cells carrying the
586 P_{MET3}-*CDC20*, following by degradation of SMCs with 1mM auxin for 1 hour prior to imaging.
587 Auxin being diluted in ethanol (EtOH), controls with EtOH only were performed **(b)** Growth
588 phenotypes on solid medium with or without Auxin in WT, Smc5-AID, Smc6-AID and Smc1-
589 AID **(c)** Representative results from immunoblotting showing the degradation of the Smc5
590 upon 30 minutes of treatment with 1 mM auxin. Actin was used as a loading control. Blots are
591 representative of three experiments. **(d-e)** MSDs as a function of increasing time intervals in
592 the absence of auxin (dark blue) and in the presence of Auxin (light blue) in a locus at 11kb
593 from the CEN4 in **(d)** Smc5-AID, Smc6-AID and **(e)** Smc1-AID. Wilcoxon rank-sum test results
594 between distributions, with the p-value *** (p<0.0001). **(f)** Table summarizing the different
595 conditions with values extracted from the MSD: MSD at 10 sec, the anomalous exponent
596 (alpha), the sub-diffusive coefficient (D) and the number of cells analyzed.

597 **Figure S6. Weakening the microtubule tether to the kinetochore gradually abolishes**
598 **position-dependent mobility:** Sweep of the wiggle distance (wd) of the bond connecting the
599 centromere to the spindle pole body (See methods for a mathematical definition of wd. In the
600 absence of other forces it is $\sqrt{2}$ times the bond standard deviation). **(a)** Mean square
601 displacement (MSD) of loci 11 kb from the centromere. **(b)** MSD of loci 90 kb from the
602 centromere. Candidate loci are selected as in Fig. 4 and wild type (WT) refers to the simulation
603 in Fig. 4a.

604 **Figure S7. Increasing chromatin stiffness increases mobility globally**: Sweep of chromatin
605 stiffness by increasing the stiffness of the bond angle potential by up to a factor two. **(a)** Loci
606 11kb from the centromere **(b)** Loci 90kb from the centromere. Candidate loci are selected as
607 in Fig. 4 and wild type (WT) refers to the simulation in Fig. 4a.

608 **Figure S8. Combining chromatin stiffness and loosening the kinetochore tether further**
609 **increases mobility in the pericentromeric region: Sweep of chromatin stiffness as** in Fig. S7
610 but with a wiggle distance (wd) of 105 nm on the bond connecting the centromere and the
611 spindle pole body. Candidate loci are 11 kb from the centromere and selected as in Fig. 4.
612 Wild type (WT) refers to the simulation in Fig. 4a.

613 **Figure S9. Smc5-2KE mutation affects HR at pericentromeres without affecting Smc5/6**
614 **chromatin loading (a)** I-*Sce*I efficiency (%) after 0h, 2h, 4h and 6h after inducing the I-*Sce*I with
615 galactose in Smc5 WT and *smc5-2KE* for centromeric (C)and luminal (L) strains. qPCR was done
616 using primers flanking the I-*Sce*I cutting site and actin was used as a loading control. The error
617 bars represent the standard deviation of three independent experiments. **(b-c)** Chromosomal
618 association of Smc5-MYC and Smc5-2KE-MYC at selected chromosomal positions as
619 determined by ChIP-qPCR for **(b)** the C strain and **(c)** the L strain. Chromosomal positions from
620 the DSB are indicated in the X-axis. T-test was used to analyze differences between groups,
621 with "ns" for not significant (P>0.05) and * for P<0.01. **(d)** I-*Sce*I efficiency (%) of the Smc5 and
622 *smc5-2KE* for C and L strains, used for local mobility. **(e)** Table summarizing the different
623 conditions with values extracted from the MSD for the fourth strains used in local mobility: C
624 WT, C *smc5-2KE,* L WT and L *smc5-2KE*: MSD at 10 sec, the anomalous exponent (alpha), the
625 sub-diffusive coefficient (D) and the number of cells analyzed.

626

627 ## References

628 1. Misteli, T. The Self-Organizing Genome: Principles of Genome Architecture and
629 Function. *Cell* **183**, 28–45 (2020).
630 2. Biggins, S. The Composition, Functions, and Regulation of the Budding Yeast
631 Kinetochore. *Genetics* **194**, 817 (2013).
632 3. Talbert, P. B. & Henikoff, S. What makes a centromere? *Exp. Cell Res.* **389**, 111895
633 (2020).
634 4. Bloom, K. Chromosome segregation: Brushing up on centromeres. *Curr. Biol.* **34**, R565–
635 R567 (2024).
636 5. Harasymiw, L. A., Tank, D., McClellan, M., Panigrahy, N. & Gardner, M. K. Centromere
637 mechanical maturation during mammalian cell mitosis. *Nat. Commun. 2019 101* **10**, 1–
638 21 (2019).
639 6. Stephens, A. D., Haase, J., Vicci, L., Taylor, R. M. & Bloom, K. Cohesin, condensin, and
640 the intramolecular centromere loop together generate the mitotic chromatin spring. *J.*
641 *Cell Biol.* **193**, 1167 (2011).
642 7. Paldi, F. *et al.* Convergent genes shape budding yeast pericentromeres. *Nat. 2020*
643 *5827810* **582**, 119–123 (2020).
644 8. D'Ambrosio, C. *et al.* Identification of cis-acting sites for condensin loading onto
645 budding yeast chromosomes. *Genes Dev.* **22**, 2215 (2008).
646 9. Jeppsson, K. *et al.* The Chromosomal Association of the Smc5/6 Complex Depends on
647 Cohesion and Predicts the Level of Sister Chromatid Entanglement. *PLoS Genet.* **10**,
648 e1004680 (2014).
649 10. Tanaka, T., Cosma, M. P., Wirth, K. & Nasmyth, K. Identification of cohesin association
650 sites at centromeres and along chromosome arms. *Cell* **98**, 847–858 (1999).
651 11. Megee, P. C., Mistrot, C., Guacci, V. & Koshland, D. The centromeric sister chromatid
652 cohesion site directs Mcd1p binding to adjacent sequences. *Mol. Cell* **4**, 445–450
653 (1999).
654 12. Lawrimore, J. & Bloom, K. Shaping centromeres to resist mitotic spindle forces. *J. Cell*
655 *Sci.* **135**, jcs259532 (2022).
656 13. Pradhan, B. *et al.* The Smc5/6 complex is a DNA loop-extruding motor. *Nat. 2023*
657 *6167958* **616**, 843–848 (2023).
658 14. Roy, S., Adhikary, H. & D'Amours, D. The SMC5 / 6 complex: folding chromosomes back
659 into shape when genomes take a break. *Nucleic Acids Res.* **52**, 2112–2129 (2024).
660 15. Laflamme, G. *et al.* Structural maintenance of chromosome (SMC) proteins link
661 microtubule stability to genome integrity. *J. Biol. Chem.* **289**, 27418–27431 (2014).
662 16. Alt, A. *et al.* Specialized interfaces of Smc5/6 control hinge stability and DNA
663 association. *Nat. Commun.* **8**, 14011 (2017).
664 17. Zhao, X. & Blobel, G. A SUMO ligase is part of a nuclear multiprotein complex that
665 affects DNA repair and chromosomal organization. *Proc. Natl. Acad. Sci. U. S. A.* **102**,
666 4777 (2005).
667 18. Torres-Rosell, J. *et al.* SMC5 and SMC6 genes are required for the segregation of
668 repetitive chromosome regions. *Nat. Cell Biol.* **7**, 412–419 (2005).
669 19. Moradi-Fard, S. *et al.* Smc5/6 Is a Telomere-Associated Complex that Regulates Sir4
670 Binding and TPE. *PLoS Genet.* **12**, (2016).
671 20. Aragón, L. The Smc5/6 Complex: New and Old Functions of the Enigmatic Long-Distance
672 Relative. *Annu. Rev. Genet.* **52**, 89–107 (2018).

673 21. De Piccoli, G. *et al.* Smc5-Smc6 mediate DNA double-strand-break repair by promoting
674 sister-chromatid recombination. *Nat. Cell Biol.* **8**, 1032–1034 (2006).
675 22. Lindroos, H. B. *et al.* Chromosomal Association of the Smc5/6 Complex Reveals that It
676 Functions in Differently Regulated Pathways. *Mol. Cell* **22**, 755–767 (2006).
677 23. Phipps, J. *et al.* Cohesin complex oligomerization maintains end-tethering at DNA
678 double-strand breaks. (2023) doi:10.1101/2023.11.08.566226.
679 24. Ampatzidou, E., Irmisch, A., O'Connell, M. J. & Murray, J. M. Smc5/6 Is Required for
680 Repair at Collapsed Replication Forks. *Mol. Cell. Biol.* **26**, 9387–9401 (2006).
681 25. Bermúdez-López, M. *et al.* The Smc5/6 complex is required for dissolution of DNA-
682 mediated sister chromatid linkages. *Nucleic Acids Res.* **38**, 6502 (2010).
683 26. Pebernard, S., Wohlschlegel, J., Mcdonald, W. H., Yates Iii, J. R. & Boddy, M. N. The
684 Nse5-Nse6 Dimer Mediates DNA Repair Roles of the Smc5-Smc6 Complex. *Mol. Cell.*
685 *Biol.* **26**, 1617–1630 (2006).
686 27. Symington, L. S. & Gautier, J. Double-strand break end resection and repair pathway
687 choice. *Annu. Rev. Genet.* **45**, 247–271 (2011).
688 28. García Fernández, F. *et al.* Modified chromosome structure caused by phosphomimetic
689 H2A modulates the DNA damage response by increasing chromatin mobility in yeast. *J.*
690 *Cell Sci.* **134**, (2021).
691 29. Herbert, S. *et al.* Chromatin stiffening underlies enhanced locus mobility after DNA
692 damage in budding yeast . *EMBO J.* **36**, 2595–2608 (2017).
693 30. Panja, D. & Barkema, G. T. Rouse modes of self-avoiding flexible polymers. *J. Chem.*
694 *Phys.* **131**, (2009).
695 31. Cabal, G. G. *et al.* SAGA interacting factors confine sub-diffusion of transcribed genes
696 to the nuclear envelope. *Nature* **441**, 770–773 (2006).
697 32. Hajjoul, H. *et al.* High-throughput chromatin motion tracking in living yeast reveals the
698 flexibility of the fiber throughout the genome. *Genome Res.* **23**, 1829–1838 (2013).
699 33. Neumann, F. R. *et al.* Targeted INO80 enhances subnuclear chromatin movement and
700 ectopic homologous recombination. *Genes Dev.* **26**, 369–383 (2012).
701 34. Verdaasdonk, J. S. *et al.* Centromere tethering confines chromosome domains. *Mol.*
702 *Cell* **52**, 10.1016/j.molcel.2013.10.021 (2013).
703 35. Wang, Z. A. & Cole, P. A. The Chemical Biology of Reversible Lysine Post-Translational
704 Modifications. *Cell Chem. Biol.* **27**, 953 (2020).
705 36. García Fernández, F. *et al.* The Dynamic Behavior of Chromatin in Response to DNA
706 Double-Strand Breaks. *Genes (Basel).* **13**, 215 (2022).
707 37. Hauer, M. H. & Gasser, S. M. Chromatin and nucleosome dynamics in DNA damage and
708 repair. *Genes Dev.* **31**, 2204–2221 (2017).
709 38. Lisby, M., Rothstein, R. & Mortensen, U. H. Rad52 forms DNA repair and recombination
710 centers during S phase. *Proc. Natl. Acad. Sci.* **98**, 8276–8282 (2001).
711 39. Pellicioli, A. *et al.* Activation of Rad53 kinase in response to DNA damage and its effect
712 in modulating phosphorylation of the lagging strand DNA polymerase. *EMBO J.* **18**,
713 6561–6572 (1999).
714 40. Shroff, R. *et al.* Distribution and Dynamics of Chromatin Modification Induced by a
715 Defined DNA Double-Strand Break. *Curr. Biol.* **14**, 1703–1711 (2004).
716 41. Peng, X. P. *et al.* Acute Smc5/6 depletion reveals its primary role in rDNA replication by
717 restraining recombination at fork pausing sites. *PLoS Genet.* **14**, (2018).
718 42. Cheblal, A. *et al.* DNA Damage-Induced Nucleosome Depletion Enhances Homology
719 Search Independently of Local Break Movement. *Mol. Cell* **80**, 311-326.e4 (2020).

720 43. Costantino, L., Hsieh, T.-H. S. H. S., Lamothe, R., Darzacq, X. & Koshland, D. Cohesin
721 residency determines chromatin loop patterns. *Elife* **9**, 1–31 (2020).
722 44. Dauban, L. *et al.* Regulation of Cohesin-Mediated Chromosome Folding by Eco1 and
723 Other Partners. *Mol. Cell* **77**, 1279-1293.e4 (2020).
724 45. Amitai, A., Seeber, A., Gasser, S. M. & Holcman, D. Visualization of Chromatin
725 Decompaction and Break Site Extrusion as Predicted by Statistical Polymer Modeling of
726 Single-Locus Trajectories. *Cell Rep.* **18**, 1200–1214 (2017).
727 46. Marshall, W. F. *et al.* Interphase chromosomes undergo constrained diffusional motion
728 in living cells. *Curr. Biol.* **7**, 930–939 (1997).
729 47. Strecker, J. *et al.* DNA damage signalling targets the kinetochore to promote chromatin
730 mobility. *Nat. Cell Biol.* **18**, 281–290 (2016).
731 48. Wigge, P. A. & Kilmartin, J. V. The Ndc80p complex from Saccharomyces cerevisiae
732 contains conserved centromere components and has a function in chromosome
733 segregation. *J. Cell Biol.* **152**, 349–360 (2001).
734 49. Lechner, J. & Carbon, J. A 240 kd Multisubunit Protein Complex, CBF3, Is a Major
735 Component of the Budding Yeast Centromere. *Cell* **64**, 717–725 (1991).
736 50. Hauer, M. H. *et al.* Histone degradation in response to DNA damage enhances
737 chromatin dynamics and recombination rates. *Nat. Struct. Mol. Biol.* **24**, 99–107 (2017).
738 51. Agmon, N., Liefshitz, B., Zimmer, C., Fabre, E. & Kupiec, M. Effect of nuclear
739 architecture on the efficiency of double-strand break repair. *Nat. Cell Biol.* **15**, 694–699
740 (2013).
741 52. Lee, C.-S. S. *et al.* Chromosome position determines the success of double-strand break
742 repair. *Proc. Natl. Acad. Sci. U. S. A.* **113**, E146–E154 (2016).
743 53. Batté, A. *et al.* Recombination at subtelomeres is regulated by physical distance,
744 double-strand break resection and chromatin status. *EMBO J.* **36**, 2609 (2017).
745 54. García Fernández, F. *et al.* Global chromatin mobility induced by a DSB is dictated by
746 chromosomal conformation and defines the HR outcome. *Elife* **11**, 1–25 (2022).
747 55. Lawrimore, J. *et al.* Microtubule dynamics drive enhanced chromatin motion and
748 mobilize telomeres in response to DNA damage. *Mol. Biol. Cell* **28**, 1701–1711 (2017).
749 56. Bouck, D. C. & Bloom, K. Pericentric Chromatin is an Elastic Component of the Mitotic
750 Spindle. *Curr. Biol.* **17**, 741 (2007).
751 57. He, X., Asthana, S. & Sorger, P. K. Transient Sister Chromatid Separation and Elastic
752 Deformation of Chromosomes during Mitosis in Budding Yeast. *Cell* **101**, 763–775
753 (2000).
754 58. Maskell, D. P., Hu, X. W. & Singleton, M. R. Molecular architecture and assembly of the
755 yeast kinetochore MIND complex. *J. Cell Biol.* **190**, 823 (2010).
756 59. Norden, C. *et al.* The NoCut Pathway Links Completion of Cytokinesis to Spindle
757 Midzone Function to Prevent Chromosome Breakage. *Cell* **125**, 85–98 (2006).
758 60. Richmond, D., Rizkallah, R., Liang, F., Hurt, M. M. & Wang, Y. A Highlights from MBoC
759 Selection: Slk19 clusters kinetochores and facilitates chromosome bipolar attachment.
760 *Mol. Biol. Cell* **24**, 566 (2013).
761 61. Davidson, I. F. *et al.* DNA loop extrusion by human cohesin. *Science (80-.).* **366**, 1338–
762 1345 (2019).
763 62. Ganji, M. *et al.* Real-time imaging of DNA loop extrusion by condensin. *Science (80-.).*
764 **360**, 102–105 (2018).
765 63. Gache, V. *et al.* Xenopus Meiotic Microtubule-Associated Interactome. *PLoS One* **5**,
766 9248 (2010).

767 64. Verdaasdonk, J. S., Gardner, R., Stephens, A. D., Yeh, E. & Bloom, K. Tension-dependent
768 nucleosome remodeling at the pericentromere in yeast. *Mol. Biol. Cell* **23**, 2560–2570
769 (2012).
770 65. Serrano, D. *et al.* The Smc5/6 Core Complex Is a Structure-Specific DNA Binding and
771 Compacting Machine. *Mol. Cell* **80**, 1025-1038.e5 (2020).
772 66. Gutierrez-Escribano, P. *et al.* Purified Smc5/6 Complex Exhibits DNA Substrate
773 Recognition and Compaction. *Mol. Cell* **80**, 1039-1054.e6 (2020).
774 67. Dion, V., Kalck, V., Seeber, A., Schleker, T. & Gasser, S. M. Cohesin and the nucleolus
775 constrain the mobility of spontaneous repair foci. *EMBO Rep.* **14**, 984–991 (2013).
776 68. Bouck, D. C. & Bloom, K. S. The kinetochore protein Ndc10p is required for spindle
777 stability and cytokinesis in yeast. *Proc. Natl. Acad. Sci. U. S. A.* **102**, 5408 (2005).
778 69. Fujioka, Y., Kimata, Y., Nomaguchi, K., Watanabe, K. & Kohno, K. Identification of a
779 novel non-structural maintenance of chromosomes (SMC) component of the SMC5-
780 SMC6 complex involved in DNA repair. *J. Biol. Chem.* **277**, 21585–21591 (2002).
781 70. Mendoza, M. *et al.* A mechanism for chromosome segregation sensing by the NoCut
782 checkpoint. *Nat. Cell Biol.* **11**, 477–483 (2009).
783 71. Potts, P. R., Porteus, M. H. & Yu, H. Human SMC5/6 complex promotes sister chromatid
784 homologous recombination by recruiting the SMC1/3 cohesin complex to double-
785 strand breaks. *EMBO J.* **25**, 3377–3388 (2006).
786 72. Roy, M.-A. A., Siddiqui, N. & D'Amours, D. Dynamic and selective DNA-binding activity
787 of Smc5, a core component of the Smc5-Smc6 complex. *Cell Cycle* **10**, 690–700 (2011).
788 73. Torres-Rosell, J. *et al.* The Smc5-Smc6 complex and SUMO modification of Rad52
789 regulates recombinational repair at the ribosomal gene locus. *Nat. Cell Biol.* **9**, 923–931
790 (2007).
791 74. Caridi, C. P. *et al.* Nuclear F-actin and myosins drive relocalization of heterochromatic
792 breaks HHS Public Access. *Nature* **559**, 54–60 (2018).
793 75. Ryu, T. *et al.* Heterochromatic breaks move to the nuclear periphery to continue
794 recombinational repair. *Nat. Cell Biol.* **17**, 1401 (2015).
795 76. Oshidari, R. *et al.* Nuclear microtubule filaments mediate non-linear directional motion
796 of chromatin and promote DNA repair. *Nat. Commun.* **9**, (2018).
797 77. Venegas, A. B., Natsume, T., Kanemaki, M. & Hickson, I. D. Inducible Degradation of the
798 Human SMC5/6 Complex Reveals an Essential Role Only during Interphase. *Cell Rep.*
799 **31**, 107533 (2020).
800 78. Therizols, P. *et al.* Chromosome arm length and nuclear constraints determine the
801 dynamic relationship of yeast subtelomeres. *Proc. Natl. Acad. Sci. U. S. A.* **107**, 2025–
802 2030 (2010).
803
804

805 # Methods

806 ## Yeast strains

807 *S. cerevisiae* strains used in this study are detailed in **Table 1** and isogenic to BY4741.

808 ## Strain construction

809 Mutations of K624E and K631E of *SMC5* were performed with CRISPR/Cas9 using a 80 pb
810 donor carrying the desired mutations as described in [54]. Unique duplexed 20 nucleotides long
811 primers next to the PAM sequence (AGG) close to K631 (oACS13/14) were cloned into a
812 replicative Cas9-KANMX plasmid (pEF562, Addgene plasmid #100955) to yield (pEF590)
813 verified by PCR and sequencing. Equimolar amounts of pEF590 and the 80 pb donor (oACS69)
814 were used to transform the desired strains and the corresponding smc5-2KE transformants
815 were verified by sequencing. The same strategy was used to obtain smc5-2KA and smc5-2KR
816 with different donor sequences carrying the specific mutation (oACS97 and oACS270
817 respectively).

818 The strains used to track the local mobility of a DSB were constructed as described in [54].
819 Briefly, the I-*Sce*I cutting site was inserted at the desired position, by replacing a KANMX
820 cassette integrated into intergenic regions of chromosome IV at positions 453880-453959 (C
821 strain) or 853996-854075 (L strain) with an mCherry sequence containing the I-*Sce*I cutting
822 site. LacO repeats at 10 kb from the cutting site were introduced by replacing a KANMX
823 cassette integrated at positions 462252-462602 (strain C) or 844554-844952 (strain L) with
824 pEF222 plasmid digested by *Bgl*II (BioLabs, R0144). LacI-GFP was introduced by digesting
825 plasmid pEF569 [78] with *Nhe*I (BioLabs, R3131). The ARS-CEN-HIS3 plasmid (pB07, obtained
826 from B. Pardo) for I-*Sce*I expression under inducible pGAL1-10 promoter, was used after
827 insertion of a stop codon in the *HIS3* genomic sequence by CrispR/Cas9 as above. The 20
828 nucleotides duplex oligos (oACS204/205) next to the PAM (TGG) sequence in *HIS3* and an 80
829 pb primer (oACS208) donor were used.

830 Depletion of *SMC5* was obtained by using a degron AFB2 based inducible [79]. AID-9MYC tag at
831 the C-terminus of *SMC5* was introduced by homologous recombination using pEF565 [80] and

832 (oACS40/53) oligonucleotides. AFB2 was introduced at the *HIS3* locus by digesting the plasmid
833 pEF604 (obtained from T.Teixeira) carrying *AFB2-HIS3* by *Nhe*I (BioLabs, R3131).

834 ## Media and growth conditions

835 Cells were grown in SC medium (2 g/l amino acids mix, 20 g/l sugar, 6.7 g/l yeast nitrogen
836 base) until they reached the mid-log phase. Multiple DNA damages were induced with 250
837 µg/ml Zeocin (Thermo Fisher, R25001) added for 4 hours (Herbert *et al.,* 2014). Microtubules
838 were depolymerized using 15 ng/µl of nocodazole (Sigma, M1404) dissolved in DMSO, for 30
839 minutes. Depolymerization was checked in parallel by Tub2-GFP disappearance in strain
840 YPT257 [78]. To induce a single DSB, 2% of galactose was added for 6 hours.

841 G1 arrest was performed using 50 ng/ml of alpha-factor (Zymo Research, Y1001M) in *Δbar1*
842 deleted strains during 3 hours prior to imaging. G2/M arrest in metaphase was done through
843 P_{MET3}-*CDC20* [7]depletion with 2 mM methionine added 2 hours before imaging. G2/M arrest in
844 prometaphase was performed with nocodazole (Sigma, M1404), 20 ng/µl during 1h and 10
845 ng/µl for an additional hour. Smc5, Smc6 or Smc1 degradation was obtained by adding 1mM
846 of auxin (Sigma, I3750-5G-A), dissolved in Ethanol 100%, 1 hour to the culture before imaging.

847 ## MT binding and cell proliferation assays

848 The affinity of Smc5 hinge domain (residues 215 to 885) for MT polymers was monitored using
849 a pelleting assay, as previously published [15]. The proliferation phenotype of cells expressing
850 wild-type and smc5 mutants was assessed by spotting 5-fold dilutions of yeast cultures on the
851 surface of solid medium and monitoring yeast growth at the indicated temperatures after 2-
852 4 days incubation at various temperatures [15].

853 ## Co-immunoprecipitation (co-IP) of Smc5/6 complex subunits

854 The co-IP was performed as described in (Roy et al., 2024; under revision at eLife) with minor
855 modifications. Yeast cultures (50mL) were grown at 30°C in YEPD medium to an optical density
856 (OD_{600}) of 0.7–0.8. Cells were harvested and lysed with glass beads in co-IP lysis buffer (50mM
857 HEPES – KOH pH 7.5, 140mM NaCl, 1% Triton X-100, 0.1% sodium deoxycholate, 1mM EDTA
858 pH 8.0, 1mM AEBSF, 10µM Pepstatin-A, 10µM E64). The purification resin (StrepTactin XT®)
859 was washed with sterile water and PBS-BSA buffer (1x PBS [phosphate buffered saline], 1%

860 BSA) just prior to the co-IP experiment. Cell lysates were cleared by centrifugation (30 minutes
861 at 13,000rpm) and combined (1mL) with the washed resin for an overnight incubation (~12h)
862 at 4°C with gentle rotation (20rpm). The resin was subsequently washed in sequence with 1)
863 co-IP lysis buffer, 2) high salt buffer (50mM HEPES – KOH pH 7.5, 360mM NaCl, 1% Triton X-
864 100, 0.1% Sodium deoxycholate, 1mM EDTA pH 8.0) and 3) TE buffer (10 mM Tris-HCl pH 8.0,
865 0.1 mM EDTA). The purification resin was finally resuspended in 2X SDS-PAGE sample buffer
866 and heated at 95°C for 5 minutes to elute purified proteins. The eluted proteins were
867 separated on a SDS-polyacrylamide gel [4-12% Bis-Tris gel ran with 1x MOPS electrophoresis
868 buffer (20mM MOPS [3-(N-Morpholino) propanesulfonic acid], 5mM of sodium acetate, 1mM
869 of disodium EDTA [isodium ethylenediaminetetraacetate dihydrate]) for 2h at 120 volts,
870 before being transferred to a membrane and analysed by immunoblotting using a 1:2,000
871 dilution of mouse anti-Strep antibody and 1:5,000 dilution of mouse anti-Myc (9E10) antibody
872 (GeneTex 369661).

873 Cell cycle time course experiment

874 To assess the kinetics of cell cycle progression, a time course experiment was performed as
875 previously described [81]. Specifically, yeast strains were grown in YPD medium at 30°C until
876 they reached an OD_{600} of 0.3-0.4. Alpha factor was then added (5µg/mL) to the medium and,
877 after 1h of growth, a second dose (2µg/mL) was added to ensure optimal arrest in G1. Once
878 ≥ 90% of the cells were synchronized in G1, they were released at 30°C in fresh YEPD medium.
879 Alpha factor (5µg/mL) was added 45 minutes after the initial release to prevent cell cycle re-
880 entry after completion of the first mitosis. For each time point, 1.5ml of cells were collected
881 and pelleted for 2 minutes at 3,000rpm. Cells were then fixed in 1mL of 70% ethanol overnight
882 at 4°C. Cells were washed twice and resuspended in 0.1M KPO_4 pH7.0 buffer. DAPI (4',6-
883 diamidino-2-phenylindole; 2µg/ml) was used to stain yeast nuclei. Separation of nuclei was
884 manually counted in 100 cells per time-point (N=3). Fluorescent images were taken using a
885 Nikon Eclipse Ti2 inverted microscope, with an 100x oil immersion objective.

886

887

888

889 ## Flow cytometry

890 Yeast cells were grown in SC selective medium overnight at 30°C, diluted to O.D_{600} nm = 0,5
891 in 5 ml next morning for 1h30 at 30°C. If necessary, cells were arrested at G1 or G2/M. 10^7
892 cells were centrifuged, fixed in 200 µl 70% ethanol and stored at 4°C for 48h. To perform FACS,
893 cells were centrifuged at 10.000 rpm 5 minutes at 4°C, washed and resuspended in 1 ml of
894 sodium citrate (50mM, pH7). 200 µl cells were transferred in polystyrene round-bottom tubes
895 with 20 µL of RNaseA (10 mg/ml Roche, 10109169001) and incubated 1 h at 37°C. Cells were
896 resuspended in 2 ml of sodium citrate (50mM, pH7) with 2.5 µM of SYTOX™ Green nucleic
897 acid stain (Sigma, S7020). Cells were stained 1h at 4°C in the dark for 1 hour. Cells were and
898 analysed with the Attune NxT Flow cytometer.

899 ## Microscopy

900 For microscopy, cells were grown as for FACS. Cells were plated on agarose patches (made of
901 SC medium containing 2% agarose) and sealed using VaLaP (1/3 Vaseline, 1/3 Lanoline and
902 1/3 Paraffin). Cells were imaged using a widefield microscopy system Nikon Ti-E equipped
903 with the Perfect Focus System (PFS) and a 60x oil immersion objective (Nikon, Plan APO).
904 Andor Neo Scmos camera allowed a vision field of 276x233 µm with a pixel size of 108 nm.
905 Fluorochromes were excited with 35% LED with a wavelength of 477 nm for GFP or 40% LED
906 with a wavelength of 587 nm for mCherry.

907 ## Dynamic analysis

908 Analyses of chromatin mobility were performed as described in Herbert et al., 2017. Briefly,
909 GFP tracking was performed by video microscopy for 3 minutes with an interval time of 100
910 ms in two dimensions (x,y). A Fiji plugin was used to isolate and extract locus trajectory at
911 each time point throughout the film. After drift correction and signal-to-noise ratio checked
912 with MATLAB scripts, Mean square distances (MSDs) for each trajectory were calculated and
913 concatenated. Power laws to the mean MSD of a population over time intervals between 0.1
914 and 10s were adapted with MATLAB script and graphs of averaged MSDs were plotted in
915 linear.

For each single locus trajectory sampled at a time resolution δt for an overall time T, the MSD at time Δt is calculated as the time-average over the $M = \frac{T-\Delta t}{\delta t}$ frames of the squared displacement performed by the locus between a running initial time $m\delta t$ and the increased time $m\delta t + \Delta t$:

$$\mathrm{MSD}_i(\Delta t) = \frac{1}{M}\sum_{m=1}^{M}\left|\vec{r}_i(m\delta t + \Delta t) - \vec{r}_i(m\delta t)\right|^2,$$

For an ensemble of N trajectories (cells), one gets an ensemble of N $MSD_i(\Delta t)$ curves; the index i therefore refers to i-th the trajectory. Each single curve can then be fitted to a $y(\Delta t) = D\Delta t^{\alpha}$ function leading to a value of the exponent α. The distribution of the ensemble of the values of α obtained is shown in Fig. 1d. In principle, the sub-diffusion coefficient D is also obtained by the same fitting procedure. However, we found that an equivalent, but more robust estimate of the sub-diffusion coefficient is obtained by the trend of the MSD over the very first 15 points, as $D = \frac{MSD_i(15\delta t)}{15\delta t}$. The D histograms of Fig. 1d refer to this definition of the sub-diffusive coefficient.

The MSD can also be averaged over the ensemble of N trajectories (cells) as

$$MSD(\Delta t) = \frac{1}{N}\sum_{i=1}^{N} MSD_i(\Delta t) = \frac{1}{N}\sum_{i=1}^{N}\frac{1}{M}\sum_{m=1}^{M}\left|\vec{r}_i(m\delta t + \Delta t) - \vec{r}_i(m\delta t)\right|^2,$$

corresponding to the curves of Fig. 1c.

Distances analysis

The analysis of distances between two differently labelled dots (GFP and mCherry) was carried out either for intrachromosomal loci, or for a pericentromeric locus and the SPB. Acquisition of 3D z-stacks consist of 35 frames with z steps of 300 nm, illumination with two consecutive colour channels for each plane with an exposure time of 100ms using a dual band filter set. First, using images from a strain dually labelled for the same locus, chromatic aberration was corrected using the plug-in “Descriptor based registration (2d/3d)”. The 3D z-stacks were then

941 converted to 2D using a maximum intensity projection. The dots were then selected using Fiji
942 and the (x,y) coordinates of the red and green loci calculated using a home-made script on
943 Fiji, taking into account the Gaussian intensity of each fluorescent loci. Comparison of
944 distances between loci was performed using Wilcoxon rank-sum tests.

945 ## ChIP-qPCR

946 Yeast cells were grown either in YPD medium or SC-His Raff 2% overnight at 30ºC. Next
947 morning, cells were diluted to a $O.D_{600}$ nm of 0,5 in 45 ml and cells were incubated at 30ºC
948 during 1h30 to reach the exponential phase. To check expression of Smc5 in the whole
949 genome, cells were synchronized at G2/M phase using nocodazole (Sigma, M1404,).
950 Nocodazole (cci. 2 mg/mL) was added two times during the time of synchronization, 20 ng/µL
951 during a first 1h at 30ºC and then 10 ng/µl for an additional hour at 30ºC under agitation. Cell
952 cycle arrest was verified by flow cytometry. In order to check the enrichment of Smc5 around
953 the DSB, DSB was induced to the cell cultures by addition of 2% galactose during 6 hours at
954 30ºC. 70 OD were recollected and treated with 1% formaldehyde for 12 minutes at room
955 temperature with rotation. Crosslinking was quenched by using 2,25 mL of glycine 2,5 M for
956 5 minutes with rotation. Then, samples were harvested by centrifugation at 3000 rpm for 5
957 minutes and washed twice with cold TBS 1X.

958 Cells pellet was resuspended in 1,2 ml of lysis buffer (50 mM HEPES-KOH pH7.5, 140 mM NaCl,
959 1 mM EDTA, 1% Triton-X 100, 0.1% sodium deoxycholate) supplemented with 1 mM PMSF,
960 phosphatase inhibitor, anti-protease (Roche, 04693132001) and 300 mg of glass beads
961 (Sigma, G8772) and lysed by MagNA Lyser rotor (Roche, 03359093001). The lysate was
962 obtained by centrifuging an eppendorf tube perforated with a sterile needle at 1000 rpm for
963 1 minute and recovering the extract in a new tube. The extract was transferred to a 1,5 ml
964 falcon tube and sonicated with a PICO sonicator (15x: 30 sec ON, 90 sec OFF, high intensity)
965 to obtain DNA with a range between 200 - 500 pb. After sonication cells were centrifuged for
966 10 minutes at 10.000 rpm at 4ºC and 25 µL of the supernatant was saved at -80ºC as INPUT.
967 250 µL of DNA after sonication were incubated with 1 µL of DNA carrier (ST0029, TakaRa Bio),
968 25 µL of BSA 5% (BP1600, Janssen Pharmacy) and 3,2 µg of anti-MYC antibody (Santa Cruz,
969 Biotechnology, INC) overnight at 4ºC. 30 ml of *Dynabeads™ Pan Mouse IgG* (Thermo Scientific,
970 11041) were added and incubated at 4ºC for 4 hours. Beads were washed twice with lysis

971 buffer, twice with lysis buffer + 0,36 M NaCl (50 mM HEPES-KOH pH7.5, 360 mM NaCl, 1 mM
972 EDTA, 1% Triton-X 100, 0.1% sodium deoxycholate), twice with washing buffer (10 mM Tris-
973 HCl pH8, 0.25 M LiCl, 0.5% NP40, 1 mM EDTA, 0.1% sodium deoxycholate) and once with
974 elution buffer (50 mM Tris-HCl pH8, 10 mM EDTA). The supernatant was removed and the
975 immunoprecipitated chromatin was then eluted by incubation in 250 µL TES buffer (50 Mm
976 Tris-HCl, pH 8.0; 10 mM EDTA; 0,5% SDS) for 15 minutes at 65ºC and the supernatant
977 collected, termed IP. The INPUT was mixed with 120 µl of TES buffer. Both INPUT and IP were
978 de-cross-linked at 65ºC with agitation overnight. RNA was degraded by incubation with 2µL
979 RNase A (10 mg/mL) for 1h at 37ºC. Proteins were removed by incubation with 20µL of
980 proteinase K (10 mg/mL) for 2h at 37ºC. DNA was purified by a phenol/Chloroform extraction.

981 Drop test

982 Overnight cultures were diluted to a $O.D_{600}$=0,5 and cells were incubated at 30ºC until they
983 reached the exponential phase. Serial 1:5 dilutions were plated starting with a O.D.= 0.2 using
984 the replication plate (R2383-1EA, Sigma) on SC in raffinose or in galactose to induce I-*Sce*I.
985 Plates were incubated at 30°C for 72 hours.

986 Colony formation unit (CFU)

987 To quantify the colonies formed in the absence or presence of an I-*Sce*I induced DSB, cells
988 were grown in -Ade -His + raffinose 2% liquid medium overnight at 30°C. After 24 hours, cells
989 were counted in a Malassez chamber and ~ 100 - 200 cells were spread on -Ade – His +
990 glucose (control) or + galactose plates (DSB induction). Plates were incubated at 30°C and
991 colonies were counted after 72h.

992 Western blot

993 Electrophoretic protein separation was done using Bolt™ 4-12% Bis-TrisPlus (Thermo Fisher
994 NW04122BOX) in Mini gels tanks (Life Technology) and the electrophoresis buffer was
995 NuPAGE™ MOPS or MES SDS Running buffer (MOPS: Thermo Fisher NP0001; MES: Thermo
996 Fisher, NP0002) for 24-26 minutes at 220 volts. Then, proteins were transferred in a
997 BioTrace™ nitrocellulose membrane (66485, Pall) in Mini PROTEAN Tetra System tanks (Bio
998 Rad) for 90 minutes. at 100 volts. Membranes were blocked with 5% milk in Tween-TBS and

999 then probed with 1/1000 Anti-MYC (Santa Cruz, Biotechnology), 1/1000 anti-HA (Sigma,
1000 H3663) or 1/500 anti-yH2A (Abcam, ab15083). Primary antibodies were recognized by
1001 secondary antibodies either anti-mouse or anti-rabbit IgG HRP-conjugated diluted 1/10000
1002 (Thermo Fisher A11005 and A31556). Blots were developed using the ECL plus western
1003 blotting system (GE Healthcare) during 10-30 sec.

1004 qPCR

1005 Cells were grown overnight in SC-Ade-His with 2% Raffinose at 30°C, diluted again in 2%
1006 Raffinose until they reached the mid-log phase and then, 2% galactose was added to the
1007 culture for I-SceI induction. Cells were collected at 0, 2, 4 and 6 hours after galactose
1008 induction. DNA was extracted from each sample using phenol/chloroform extraction. For this
1009 purpose, cells were centrifuged 1 minute. at 13000 rpm, the pellet was mixed with 300 mg of
1010 glass beads, 200 µL of lysis solution (Triton X-100 2 %, SDS 1 %, NaCl 100 mM, Tris 10 mM pH
1011 8, EDTA 1 mM) and 200 µL phenol-chloroform-isoamyl alcohol (Sigma, 77617). The mix was
1012 vortexed for 10 minutes at 4ºC and centrifuged for 10 minutes. at 13000 rpm at 4°C. 140 µL
1013 of the supernatant was transferred into new tubes containing 500 µL ethanol 100% and DNA
1014 was precipitated during 1 hour at 80ºC. The mix was centrifuged for 10 minutes. at 13000 rpm
1015 at 4°C. The pellet was washed with 500 µL of ethanol 70 % and dried at room temperature
1016 resuspended in 40 µL of TE containing 20 µg/µL of RNase (Roche, 10109169001) and
1017 incubated 30 minutes. at 42°C. DNA concentrations were quantified using nanodrop.

1018 qPCRs were prepared in a 360-wells plate. All samples were brought to a concentration of 5
1019 ng/µL. In each well, 4µL of the sample were mixed with 4 µL of Power Track SYBR™ Green
1020 master mix (Thermo Fisher A46109) and 0,3 µL of forward and reverses oligonucleotides (final
1021 concentration 2.10^{-5} M). Oligonucleotides are listed in **Table 2**. I-*Sce*I oligonucleotides
1022 generated a 187bp fragment that flanks the I-*Sce*I cutting site. ACT1 was used as a control to
1023 normalize the samples. The standard curve was performed on actin (control) and I-*Sce*I cutting
1024 site (before cut) to evaluate the efficiency of the couple of primers used. Triplicates from each
1025 sample were performed and four 1:5 dilutions were performed for the standard curve.

1026 Plate sampling was distributed by the epMotion 5070 robot (Eppendorf), qPCR was
1027 performed with QuanStudio5 qPCR machine (Thermo Fisher) under the following conditions:

1028 pre-incubation (95°C – 5 min – 4.4 °C/min), amplification (45 cycles; 95°C – 10 s - 4.4°C/min;
1029 58°C – 10 s - 2.2 °C/min; 72°C – 20 s – 4,4 °C/min), melting curve (95°C – 5 s - 4.4 °C/min; 60°C
1030 – 1 min – 2.2 °C/min; 97°C – continuous – 0.06 °C/min; 10 acquisitions/°C) and cooling (40°C
1031 – 30 s - 2.2 °C/ min.). qPCR was analyzed with Thermo Fisher cloud and normalized by the
1032 Livak method ($2^{\Delta\Delta Ct}$) [82].

1033 Polymer model

1034 The polymer model was identical to the one used in Liu et al. 2023 [83] which was based on the
1035 model of Arbona et al. 2017 [84] but made in Polychrom
1036 (https://github.com/open2c/polychrom/tree/master), a python wrapper for polymer
1037 simulations using openMM [85]. The model consisted of a diploid yeast nucleus where each
1038 monomer represents 750 bp and is 15 nm in radius. The monomers were connected with
1039 harmonic bonds with a spring constant parameterized by a wiggle-distance w such that bond
1040 extensions of w lead to bond energies of 1kT

1041 $$k = \frac{2k_B T}{w^2}.$$

1042 From this follows that, in the absence of other forces, the wiggle distance will be equal to $\sqrt{2}$
1043 times the bond standard deviation.

1044 The beads were allowed to interact through the soft "polynomial_repulsive" potential.
1045 Stiffness was introduced through a harmonic force on the bond angle which favored
1046 alignment. The spring constant was chosen to yield a persistence length of 70 nm which was
1047 found optimal by Arbona et al. The nuclear envelope was modeled by a spherical confinement
1048 with a 1µm radius, and all telomeres were attached to the wall using strong harmonic bonds
1049 which allowed movement along the periphery but no radial motion. All centromeres were
1050 attached to the SPB using harmonic bonds with a 400 nm rest length and a high spring
1051 constant, allowing negligible fluctuations in length. The nucleolus was modeled by inserting
1052 112,500 bp at the rDNA region where the size of monomers and bonds were increased by a
1053 factor 14. Long simulations were run to collect a set of starting configurations from which the
1054 starting conformation for short-time simulations were then randomly chosen upon

1055 initialization. The conversion factor between simulation time and experimental time was
1056 chosen to match the MSD of the 11kb loci in the WT condition.

1057

1058 # Tables

1059 Table 1: genotypes of used strains

Common name	Strain	Genotype	Reference
11kb Chr IV	YPE4019	Mata, ura3, trp1-1, leu2-3, his3-11,15, can1-100, ade2-1, P_{MET3}-CDC20::URA3, Spc42-tdTomato::Nat, leu2:: P_{URA3}-TetR-GFP::LEU2, tetOx224-URA3 (tetOs 11,5kb to right of CEN4), yil015w::KanMX	Paldi *et al* 2020
11kb-2KE Chr IV	YPE4144	Mata, ura3, trp1-1, leu2-3, his3-11,15, can1-100, ade2-1, P_{MET3}-CDC20::URA3, Spc42-tdTomato::Nat, leu2:: P_{URA3}-TetR -GFP::LEU2, tetOx224-URA3 (tetOs 11,5kb to right of CEN4), yil015w::KanMX, YOL034W::K624E, YOL034W::K631E	This study
23kb Chr IV	YEF1659	Mata, ura3, trp1-1, leu2-3, his3-11,15, can1-100, ade2-1, P_{MET3}-CDC20::URA3, Spc42-tdTomato::Nat, leu2:: P_{URA3}-TetR -GFP::LEU2, tetOX224-URA3 (tetOs 11,5kb to right of CEN4)	Paldi *et al* 2020
23kb-2KE Chr IV	YPE4145	Mata, ura3, trp1-1, leu2-3, his3-11,15, can1-100, ade2-1, P_{MET3}-CDC20, Spc42-tdTomato::Nat, leu2:: P_{URA3}-TetR -GFP::LEU2, tetOX224-URA3 (tetOs 23kb to right of CEN4), YOL034W::K624E, YOL034W::K631E	This study
90kb Chr IV	YEF1081	Mat alpha, ura3Δ0 or-851, his3Δ1, can1::HPHMX, his3::HIS3-LacI-GFP, YDR042C::lacO-LEU2	This study
90kb-2KE Chr IV	YEF1654	Mat alpha, ura3Δ0 or-851, his3Δ1, can1::HPHMX, his3::HIS3-LacI-GFP YDR042C::lacO-LEU2, YOL034W::K624E, YOL034W::K631E	This study

730kb Chr IV	YEF1068	Mat alpha, ura3Δ0, leu2Δ0, his3Δ1, lys2Δ202, ade2-661, iyGL117::TetR-mRFP-NATMX, YDR354W::tetO-URA3 HIS3::HIS3-LacI-GFP YDR259C::lacO-TLEU2	This study
730kb-2KE Chr IV	YEF1706	Mat alpha, ura3Δ0, leu2Δ0, his3Δ1lys2Δ202, ade2-661, iyGL117::tetR-mRFP NATMX YDR354W::tetO-URA3 HIS3::HIS3-LacI-GFP, YDR259C::lacO- LEU2, YOL034W::K624E, YOL034W::K631E	This study
90kb-2KA Chr IV	YEF1668	Mat alpha, ura3Δ0, trp1Δ63, leu2Δ0, his3Δ1, lys2Δ202, can1::HPHMX, ade2-661, lys2::TetR-GFP-LYS2, yel053c ::KanMX::tetO-URA3, Chr IV 453880+453959 :: KanMX:: mCherry*-I*Sce*I(cs), YOL034W::K624A, YOL034W::K631A,	This study
90kb-2KR Chr IV	YPE4180	Mat alpha, ura3Δ0, trp1Δ63, leu2Δ0, his3Δ1, lys2Δ202, can1::HPHMX, ade2-661, lys2::TetR-GFP-LYS2, yel053c ::KanMX::tetO-URA3, Chr IV 453880+453959 ::KanMX:: mCherry*-I*Sce*I(cs), YOL034W::K624R, YOL034W::K631ER	This study
90kb Chr V	YEF1454	Mat alpha, ura3Δ0, trp1Δ63, leu2Δ0, his3Δ1, lys2Δ202, can1::HPHMX, ade2-661, lys2::TetR-GFP-LYS2, yel053c ::KanMX:: tetO-URA3, Chr IV 453880+453959 ::KanMX:: mCherry*-I*Sce*I(cs)	García-Fernandez *et al.,* 2022
90kb-2KE Chr V	YEF1666	Mat alpha, ura3Δ0, trp1Δ63, leu2Δ0, his3Δ1, lys2Δ202, can1::HPHMX, ade2-661,::TetR-GFP-LYS2, yel053c ::KanMX:: tetO-URA3, Chr IV 453880+453959 :: KanMX:: mCherry*-I*Sce*I(cs), YOL034W::K624E, YOL034W::K631E	This study
SMC6-AID AFB2	YPE4059	Mat a, trp1-1, leu2-3, his3-11, ade2-1, P_{MET3}-CDC20::URA3, Spc42-tdTomato::Nat, leu2::PURA3::tetR-GFP::LEU2, tetOX224-URA3 (tetOs 11,5kb to right of CEN4), Smc5-AID-9myc-KanMX, his3-11,15 :: pEF604 (=AFB2-HIS3)	This study
SMC1-AID AFB2	YPE4173	Mat a, trp1-1, leu2-3, his3-11, ade2-1, P_{MET3}-CDC20::URA3, Spc42-tdTomato::Nat, leu2::PURA3::tetR-GFP::LEU2, tetOX224-URA3 (tetOs 11,5kb to right of CEN4), yil015w::KanMX, his3-11,15::AFB2-HIS3(pEF604), Smc6-AID-9myc-TRP1	This study

SMC5-AID AFB2	YPE4176	Mat a, trp1-1, leu2-3, his3-11, ade2-1, P_{MET3}-CDC20::URA3, Spc42-tdTomato::Nat, leu2::PURA3::tetR-GFP::LEU2, tetOX224-URA3 (tetOs 11,5kb to right of CEN4), yil015w::KanMX, his3-11,15::AFB2-HIS3(pEF604), Smc1-AID-3myc-TRP1	This study
Rad52 GFP	YEF651	Mata, ura3Δ0, leu2Δ0, his3Δ1, met15Δ0, YML032C-GFP-HIS3MX6	
Rad52-GFP 2KE	YEF1647	Mata, ura3Δ0, leu2Δ0, his3Δ1, met15Δ0, YML032C-GFP-HIS3MX6, YOL034W::K624E, YOL034W::K631E	This study
RAD53-HA	YEF954	Mat alpha, ura3-Δ851, trp1-Δ63, leu2Δ1, his3Δ200, ade2-661, yml032c::KANMX, rad53-HA	
RAD53-HA 2KE	YEF1882	Mat alpha, ura3-Δ851, trp1-Δ63, leu2Δ1, his3Δ200, ade2-661, yml032c::KANMX, rad53-HA, YOL034W::K624E, YOL034W::K631E	This study
R1	YEF1065	Mat a, ura3Δ0, leu2Δ0/, his3Δ1, lys2Δ202, ade2-661, can1::HPHMX, iyGL117::tetR-mRFP- NATMX, YDR003W::tetO-TEF-URA, HIS3::HIS3-LacI-GFP, YDR095C::256lacO-TEF-LEU2	Herbert *et al* 2017
R1 2KE	YEF1887	Mat a, ura3Δ0, leu2Δ0/, his3Δ1, lys2Δ202, ade2-661, can1::HPHMX, iyGL117::tetR-mRFP- NATMX, YDR003W::tetO-TEF-URA, HIS3::HIS3-LacI-GFP, yDR095c::256lacO-LEU2, YOL034W::K624E, YOL034W::K631E	This study
R3	YEF1068	Mat alpha, ura3Δ0, leu2Δ0, his3Δ1, lys2Δ202, ade2-661, iyGL117::tetR-mRFP-NATMX, YDR354W::tetO-TEF-URA3 HIS3::HIS3-LacI-GFP YDR259C::lacO- LEU2	Herbert *et al* 2017
R3 2KE	YEF1706	Mat alpha, ura3Δ0, leu2Δ0, his3Δ1, lys2Δ202, ade2-661, iyGL117::tetR-mRFP NATMX YDR354W::tetO-TEF-URA3 HIS3::HIS3-LacI-GFP YDR259C::lacO- LEU2, YOL034W::K624E, YOL034W::K631E	This study
Tub2-GFP	YPE257	Mata, ura3-52, trp1Δ63, leu2Δ1, lys2-801, ade2-661, ura3-52::TUB2-GFP-URA3	

Tub1-GFP SMC5-2KE	YEF1864	Mata, ura3-52, trp1Δ63, leu2Δ1, lys2-801, ade2-661, ura3-52::TUB1-GFP-URA3, YOL034W::K624E, YOL034W::K631E	This study
Smc5-ndc80-1	YEF1928	Mat alpha, ura3Δ0, trp1Δ63, leu2Δ0, his3Δ1, lys2Δ202, can1::HphMX,ade2-661, lys2::TetR-GFP-LYS2, yel053c ::KanMX:: tetO-URA3, Chr IV 453880+453959::KanMX:: mCherry*-I-*Sce*I(cs), ndc80-1	This study
ndc80-1 Smc5-2KE	YEF1930	Mat alpha, ura3Δ0, trp1Δ63, leu2Δ0, his3Δ1, lys2Δ202, can1::HphMX,ade2-661/,lys2::TetR-GFP-LYS2, yel053c ::KanMX:: tetO-URA3, Chr IV 453880+453959::KanMX:: mCherry*-I-*Sce*I(cs), YOL034W::K624E, YOL034W::K631E, ndc80-1	This study
L WT sDSB	YEF1203	Mat alpha, ura3Δ0, trp1Δ63, leu2Δ0, his3Δ1, lys2Δ202, ade2-661, lys2::TetR-GFP-LYS2, can1::HphMX, YEL053C :: KANMX:: tetO-URA Chr IV 853996+854075:: KANMX:: mCherry*-I-*Sce*I(cs)	García-Fernandez *et al.,* 2022
L 2KE sDSB	YPE4131	Mat alpha, ura3Δ0, trp1Δ63, leu2Δ0, his3Δ1, lys2Δ202, ade2-661, lys2::TetR-GFP-LYS2, can1::HPHMX, YEL053C::KanMX::tetO-URA, Chr IV 853996+854075:: KanMX:: mCherry*-I-*Sce*I(cs), YOL034W::K624E, YOL034W::K631E,	This study
C - DSB Local mobility	YPE4132	Mata,ura3Δ0,,leu2Δ0/,his3Δ1/, met15Δ0/,YOL034W-13xMYC-URA3, Chr IV 453880+453959::KanMX::mCherry*-I*Sce*I(cs), ymr008C::KanMX::lacO-LEU2, LacI-HIS3, HIS3-STOP, p2u-HIS3	This study
C + DSB Local mobility	YPE4133	Mata, ura3Δ0, leu2Δ0, his3Δ1, met15Δ0, YOL034W-13xMYC-URA3, Chr IV 453880+453959::KANMX::mCherry*-I-*Sce*I(cs), ymr008C::kanMX::lacO-LEU2, LacI-HIS3, HIS3-STOP, pGALISceI-HIS3	This study

C 2KE - DSB Local mobility	YPE4136	Mata, ura3Δ0, leu2Δ0, his3Δ1, met15Δ0, YOL034W::K624E, YOL034W::K631E, YOL034W-13xMYC-URA3, Chr IV 453880+453959::KanMX: mCherry*-I-*Sce*I(cs), ymr008C::kanMX::lacO-LEU2, LacI-HIS3, HIS3-STOP, p2u-HIS3	This study
C 2KE + DSB Local mobility	YPE4137	Mata, ura3Δ0, leu2Δ0, his3Δ1, met15Δ0, YOL034W::K624E, YOL034W::K631E, YOL034W-13xMYC-URA3, Chr IV 453880+453959::KanMX::mCherry*-I-*Sce*I(cs), ymr008C::kanMX::lacO-LEU2, LacI-HIS3, HIS3-STOP, pGALISceI-HIS3	This study
L - DSB sDSB Local mobility	YPE4134	Mata, ura3Δ0, leu2Δ0, his3Δ1, met15Δ0, YOL034W-13xMYC-URA3, Chr IV 853996+854075::KanMX::mCherry*-I-*Sce*I(cs), ydr193w::kanMX::lacO-LEU2, LacI-HIS3, HIS3-STOP, p2u-HIS3	This study
L + DSB Local mobility	YPE4135	Mata, ura3Δ0, leu2Δ0, his3Δ1, met15Δ0, YOL034W-13xMYC-URA3, Chr IV 853996+854075::KanMX::mCherry*-I-*Sce*I(cs), ydr193w::kanMX::lacO-LEU2, LacI-HIS3, HIS3-STOP, pGALISceI-HIS3	This study
L 2KE - DSB Local mobility	YPE4138	Mata, ura3Δ0, leu2Δ0, his3Δ1, met15Δ0, YOL034W::K624E, YOL034W::K631E, YOL034W-13xMYC-URA3, Chr IV 853996+854075::KanMX::mCherry*-I-*Sce*I(cs), ydr193w::kanMX::lacO-LEU2, LacI-HIS3, HIS3-STOP, p2u-HIS3	This study
L 2KE + DSB Local mobility	YPE4139	Mata, ura3Δ0, leu2Δ0, his3Δ1, met15Δ0, YOL034W::K624E, YOL034W::K631E, YOL034W-13xMYC-URA3, Chr IV 853996+854075::KanMX::mCherry*-I-*Sce*I(cs), ydr193w::kanMX::lacO-LEU2, LacI-HIS3, HIS3-STOP, pGALISceI-HIS3	This study
C - DSB ChIP-qPCR	YEF1922	Mata, ura3Δ0, leu2Δ0, his3Δ1, met15Δ0, YOL034W-13xMYC-URA3, Chr IV 853996+854075:: kanMX::mCherry*-ISceI(cs), p2u-HIS3	This study
C + DSB ChIP-qPCR	YEF1923	Mata, ura3Δ0, leu2Δ0, his3Δ1, met15Δ0, YOL034W-13xMYC-URA3, Chr IV 853996+854075::kanMX:::mCherry*-I-*Sce*I(cs), pGALISceI-HIS3	This study

C 2KE - DSB ChIP-qPCR	YEF1934	Mata, ura3Δ0, leu2Δ0, his3Δ1, met15Δ0, YOL034W::K624E, YOL034W::K631E, YOL034W-13xMYC-URA3, Chr IV 453880+453959 :: kanMX :: mCherry*-I-*Sce*I(cs), p2u-HIS3	This study
C 2KE + DSB ChIP-qPCR	YEF1925	Mata, ura3Δ0, leu2Δ0, his3Δ1, met15Δ0, YOL034W::K624E, YOL034W::K631E, YOL034W-13xMYC-URA3, Chr IV 453880+453959 :: kanMX :: mCherry*-I-*Sce*I(cs), $P_{GAL1-10}$-*I-SceI*-HIS3	This study
L - DSB ChIP-qPCR	YEF1898	Mata, ura3Δ0, leu2Δ0, his3Δ1, met15Δ0, YOL034W-13xMYC-URA3, Chr IV 853996+854075:: kanMX :: mCherry*-I-*Sce*I(cs), p2u-HIS3	This study
L + DSB ChIP-qPCR	YEF1900	Mata, ura3Δ0, leu2Δ0, his3Δ1, met15Δ0, YOL034W-13xMYC-URA3, Chr IV 853996+854075::kanMX::mCherry*-I-*Sce*I(cs), $P_{GAL1-10}$-*I-SceI*-HIS3	This study
L 2KE - DSB ChIP-qPCR	YEF1926	Mata, ura3Δ0, leu2Δ0, his3Δ1, met15Δ0, YOL034W::K624E, YOL034W::K631E, YOL034W-13xMYC-URA3, Chr IV 853996+854075::kanMX::mCherry*-I-*Sce*I(cs), p2u-HIS3	This study
L 2KE + DSB ChIP-qPCR	YEF1920	Mata, ura3Δ0, leu2Δ0, his3Δ1, met15Δ0, YOL034W::K624E, YOL034W::K631E, YOL034W-13xMYC-URA3, Chr IV 853996+854075::kanMX::mCherry*-*I-SceI*(cs), $P_{GAL1-10}$-*I-SceI*-HIS3	This study
CEN-SPB	YEF1019	Mat a, his3Δ1 or his3Δ200, lys2Δ202 or 0, cenIV-tetO-URA3, lys2Δ202::tetR-GFP-LYS2 , SPC42-mCherry-HIS3	García-Fernandez *et al.,* 2021
CEN-SPB Smc5-2KE	YEF1691	Mat a, his3Δ1 or his3Δ200, lys2Δ202 or 0, cenIV-tetO-URA3, lys2Δ202::tetR-GFP-LYS2 , SPC42-mCherry-HIS3, YOL034W::K624E, YOL034W::K631E	This study
Mtw1-3xGFP	YEF1017	Mat a, ura3-1, trp1-1, leu2Δ3,112, his3-11, can1-100, ade2-1, ura3::TUB1-CFP::URA3, YAL034W-A-3xGFP::HIS3, yil015w::KANMX	García-Fernandez *et al.,* 2021

Mtw1-3xGFP Smc5-2KE	YEF4025	Mat a, ura3-1, trp1-1, leu2Δ3,112, his3-11, can1-100, ade2-1, ura3::TUB1-CFP::URA3, YAL034W-A-3xGFP::HIS3, YOL034W::K624E, YOL034W::K631E, yil015w::KANMX	This study

1060 Table 2: primers used in this study

Gene / region	Primer	Sequence (5'→ 3')	Reference
gRNA 2KE	oACS13	CTGAAGGGCGAGATCAAGCgtttt	This study
	oACS14	CTCGTTGTGGGAGGTGATGTgatca	This study
Donor 2KE	oACS69	TCATGGGAATAGGTTAGTCGATATC**GAA**CAATCAGCATATGGTAGTgaaCAGGTCTTTCCTACTGACGTTAGTATTAAAC	This study
Donor 2KA	oACS97	TCATGGGAATAGGTTAGTCGATATC**GCG**CAATCAGCATATGGTAGT**GCG**CAAGTCTTTCCTACTGACGTTAGTATTAAAC	This study
Donor 2KR	oACS270	TCATGGGAATAGGTTAGTCGATATC**AGA**CAATCAGCATATGGTAGT**AGA**CAAGTCTTTCCTACTGACGTTAGTATTAAAC	This study
Smc5-MYC	oACS103	ATCCGAAGATGATACATTTCGGTGAAACTTCTAACTACTCATTCGAACGGATCCCCGGGttaattaa	This study
	oACS94	AAACATGTTTACATCTATATGTGTATAATTAATTATGCAATAGTGAAAGATGAATTCGAGCTCGTTTAAAC	This study
AID	oACS40	AGGATCCGAAGATGATACATTTCGGTGAAACTTCTAACTACTCATTCGATcgtacgctgcaggtcgac	This study
	oACS53	AAACATGTTTACATCTATATGTGTATAATTAATTATGCAATAGTGAAAGAatcgatgaattcgagctcg	This study
AFB2	oACS199	ACGCGCCGCTCACCCGCACGGCAGAGACCAATCAGTAAAAATCAACGGTTAATTCGGTCGAAAAAAGAAA	This study

	oACS200	AGCTTACATTTTATGTTAGCTGGTGGACTGACGCCAGAAAATGTTGGTGATTAGAGAATCCACACAAATG	This study
KanMX R1	OEA177	ACTTGGTTGGCGTGTTTCGT	This study
	OEA178	GCGGTTGTTTGCAAGACCGA	This study
KanMX R2	OEA181	GTCAAGGGCGTGTTTGACGC	This study
	OEA182	ACGAATTTTGCTCCGGCAATTCT	This study
Cherry-*I-SceI*-cs	OEA310	TAGGATACAGTTCTCACATCACATCCGAACATAAACAACCATGGTGAGCAAGGGCGA	This study
	OEA311	ATGACAAGTTCTTGAAAACAAGAATCTTTTTATTGTCAGTCTACTTGTACAGCTCGTCCATG	This study
gRNA HIS3	oACS13	GAGTGCGTTCAAGGCTCTTGgtttt	This study
	oACS14	CAAGAGCCTTGAACGCACTCgatca	This study
Donor HIS3	oACS69	GATTAACGTCCACACAGGTATAGGGTTTCTGGACCATATGATA**TAA**GCTCTGGCCAAGCATT CCGGCTGGTCGCTAATCG	This study
R1 5 Kb		GGCAATTGAGGCCTTCTGGC	García Fernandez et al., 2021
		TGGTGGCCAACGATCCTTCA	
R1 10Kb	oACS136	AGCGGAATCAGGAGTGCAAAA	This study
	oACS137	TGGAAAAATGCATCTACAACCGCT	
	oACS138	GCCAAAGGTGTTTTCATTTGGAAGG	This study

R1 15 Kb	oACS139	ACCAGCACCTGACTCTCCCA	
R1 50 Kb		TTCTCCCTTGTCACCGCCACC	García Fernandez et al., 2021
		GGCCGCTCAAGTTAACGCCCA	
R1 150 Kb		TGGGAATCGTTTTATCCTTGTTTCGC	García Fernandez et al., 2021
		GTGAAGCAACCAACATAATGCCAG	
R2 5 Kb	oACS187	TGATTCCTCTGGGAGGCGCA	This study
	oACS188	TGACAGGTGCTCTAGTGTCCG	
R2 10 Kb	oACS189	CGAAGAAGACTTAATGGTGAAGGGT	This study
	oACS190	ACAGCCTGCAACCTTAACAGCA	
R2 15 Kb	oACS191	TCGAGGCTGGTGAAGAGAAACT	This study
	oACS192	AGTGCTATTTGGTCGGGGAGA	
R2 50 Kb	oACS193	ACTGGCCTGACATAGCCCTGA	This study
	oACS194	ACGCGAGGATTTTTGTTCGTGG	

1064 Table 3: plasmids used in this study

Name	Marker	Features	Origin
pEF562	KANMX	Plasmid carrying Cas9 and a gRNA scaffold. gRNAs were introduced by digesting this plasmid with BplI.	[87]
pEF590	KANMX	Plasmid coming from the pEF562 carrying the gRNA to cut close to the SMC5-K631.	This study
pEF601	URA3	Plasmid carrying pFA6a-13MYC-URA3 used to introduce 13x MYC at the C-terminus of *SMC5*	P. Lesage
pEF222	LEU2	Plasmid carrying pTEF-tTEF-LEU2-LacO, used to integrate the LacO in the place of a KanMX	Therizols et al., 2010
pEF569	HIS3	Plasmid carrying LacI-GFP-HIS3, which was linearized with *NheI* to introduce LacI-GFP into *HIS3*	
pEF604	HIS3	Plasmid carrying the AFB2, which was linearized with *NheI* to introduce AFB2-URA3 into *URA3*.	T. Teixeira
pEF608	HIS3	Plasmid coming from the pJH2970 (Addgene, 100954) carrying the gRNA to cut close to the Smc5-K631.	This study
pB07	HIS3	Plasmid carrying the I-*Sce*I enzyme under GAL1-10 promoter	García-Fernandez et al 2022
pEF573	ADE2	Centromeric plasmid carrying the mCherry donor sequence, without the promoter and terminator.	García-Fernandez et al 2022

1065

1066 ## References

1067 79. Nishimura, K. & Kanemaki, M. T. Rapid Depletion of Budding Yeast Proteins via the
1068 Fusion of an Auxin-Inducible Degron (AID). *Curr. Protoc. cell Biol.* **64**, 20.9.1-20.9.16
1069 (2014).
1070 80. Morawska, M. & Ulrich, H. D. An expanded tool kit for the auxin-inducible degron
1071 system in budding yeast. *Yeast* **30**, 341–351 (2013).
1072 81. Ratsima, H. *et al.* Independent modulation of the kinase and polo-box activities of Cdc5
1073 protein unravels unique roles in the maintenance of genome stability. *Proc. Natl. Acad.*
1074 *Sci. U. S. A.* **108**, (2011).
1075 82. Livak, K. J. & Schmittgen, T. D. Analysis of Relative Gene Expression Data Using Real-
1076 Time Quantitative PCR and the 2−ΔΔCT Method. *Methods* **25**, 402–408 (2001).
1077 83. Liu, S. *et al.* In vivo tracking of functionally tagged Rad51 unveils a robust strategy of
1078 homology search. *Nat. Struct. Mol. Biol.* **30**, 1582–1591 (2023).
1079 84. Arbona, J. M., Herbert, S., Fabre, E. & Zimmer, C. Inferring the physical properties of
1080 yeast chromatin through Bayesian analysis of whole nucleus simulations. *Genome Biol.*
1081 **18**, (2017).
1082 85. Eastman, P. *et al.* OpenMM 7: Rapid development of high performance algorithms for
1083 molecular dynamics. *PLOS Comput. Biol.* **13**, e1005659 (2017).

1084

Fig. 1

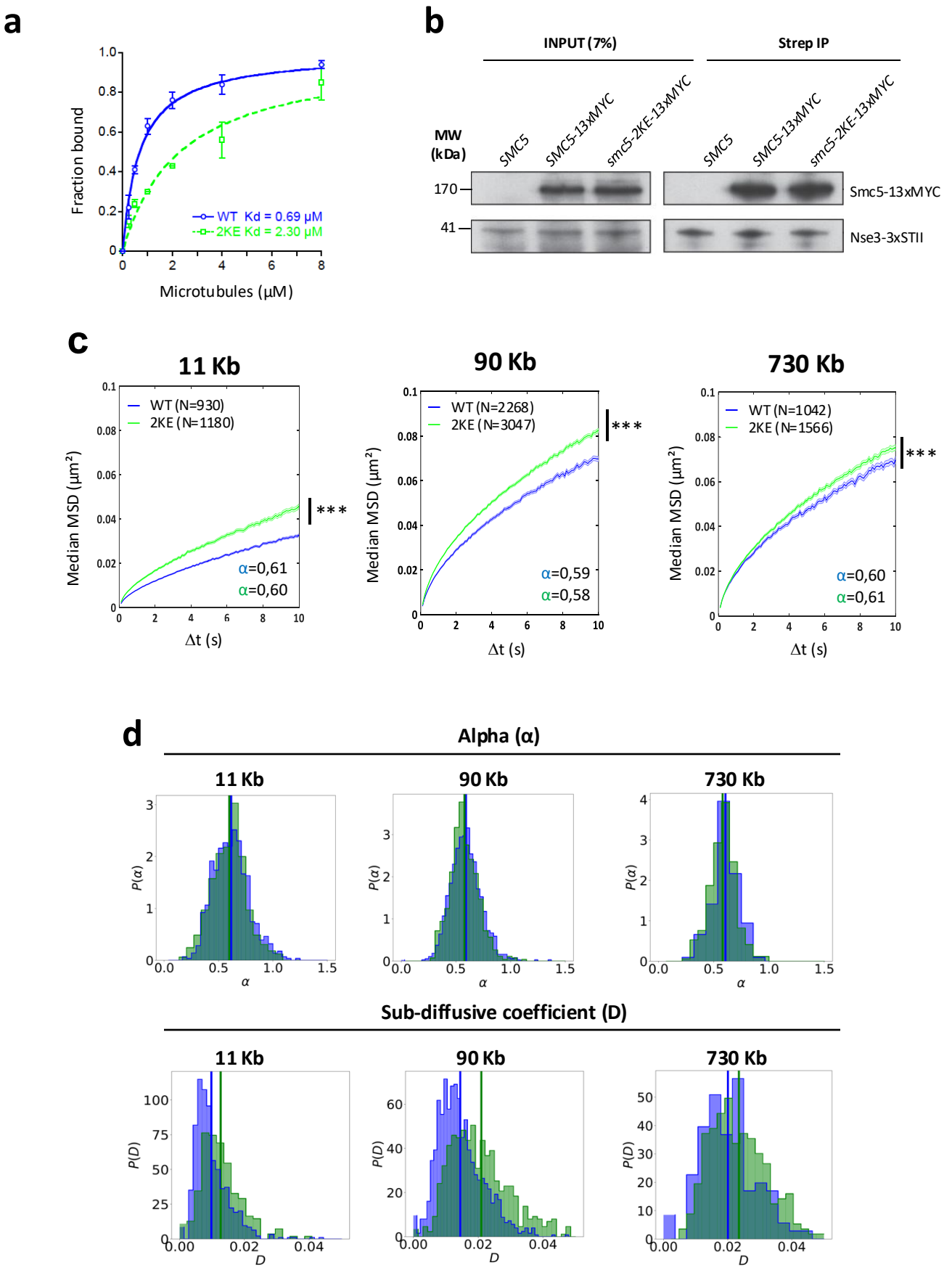
a
Fraction bound
Microtubules (µM)
WT Kd = 0.69 µM
2KE Kd = 2.30 µM
b
INPUT (7%)
Strep IP
MW (kDa)
SMC5
SMC5-13xMYC
smc5-2KE-13xMYC
170
41
Smc5-13xMYC
Nse3-3xSTII
c
11 Kb
90 Kb
730 Kb
Median MSD (µm²)
Δt (s)
WT (N=930)
2KE (N=1180)
α=0,61
α=0,60
WT (N=2268)
2KE (N=3047)
α=0,59
α=0,58
WT (N=1042)
2KE (N=1566)
α=0,60
α=0,61
***
d
Alpha (α)
P(α)
α
Sub-diffusive coefficient (D)
P(D)
D

Fig. 2

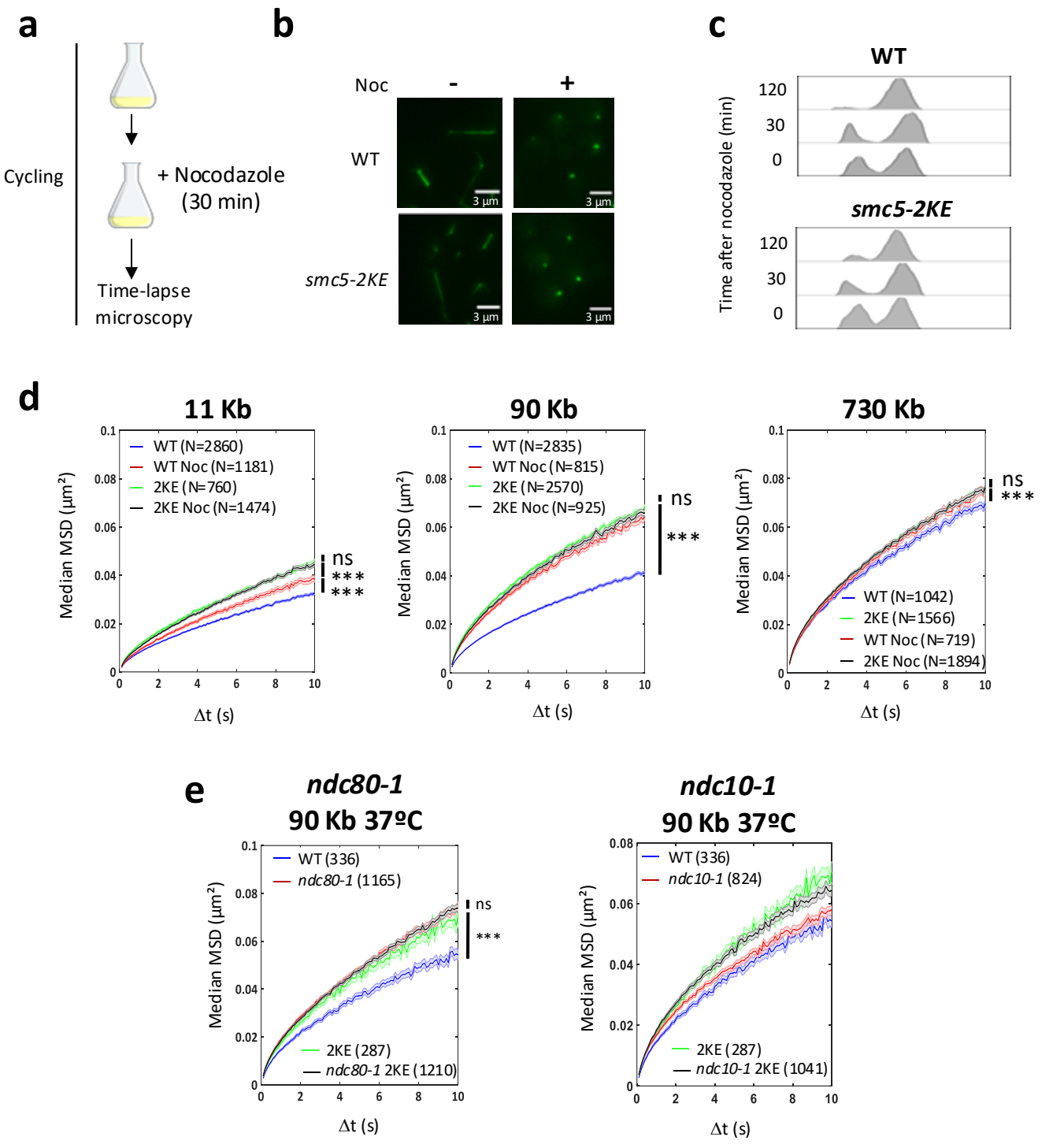

f

Cell phase	Tracked locus	Smc5 allele	MSD at 10 sec (10^{-2})	Alpha	D (10^{-3})	Cell number
Cycling + Nocodazole	11 kb	WT	3.83	0.62	2.19	760
		smc5-2KE	4.45	0.62	2.54	1474
	90 kb	WT	6.47	0.61	2.00	815
		smc5-2KE	6.58	0.60	2.70	925
	730 kb	WT	7.44	0.60	4.71	719
		smc5-2KE	7.63	0.58	5.07	1894
Cycling 37ºC	90 kb	WT	5.43	0.60	3.49	336
		ndc80-1	7.49	0.61	4.42	1165
		smc5-2KE	7.04	0.60	4.59	287
		ndc80-1 smc5-2KE	7.38	0.61	4.46	1210

Fig. 3

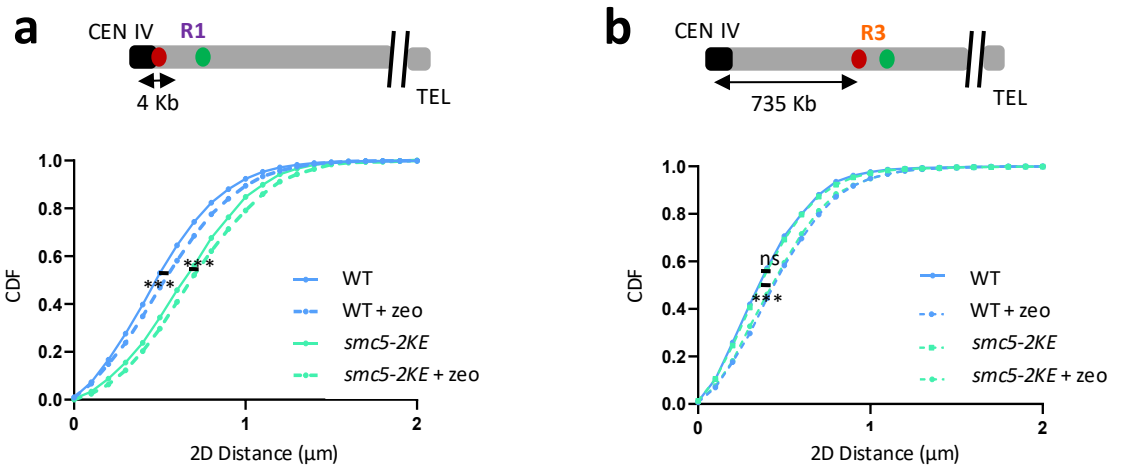
a
CEN IV
R1
4 Kb
TEL
CDF
2D Distance (µm)
***
***
WT
WT + zeo
smc5-2KE
smc5-2KE + zeo
b
CEN IV
R3
735 Kb
TEL
CDF
2D Distance (µm)
ns
***
WT
WT + zeo
smc5-2KE
smc5-2KE + zeo

Fig. 4

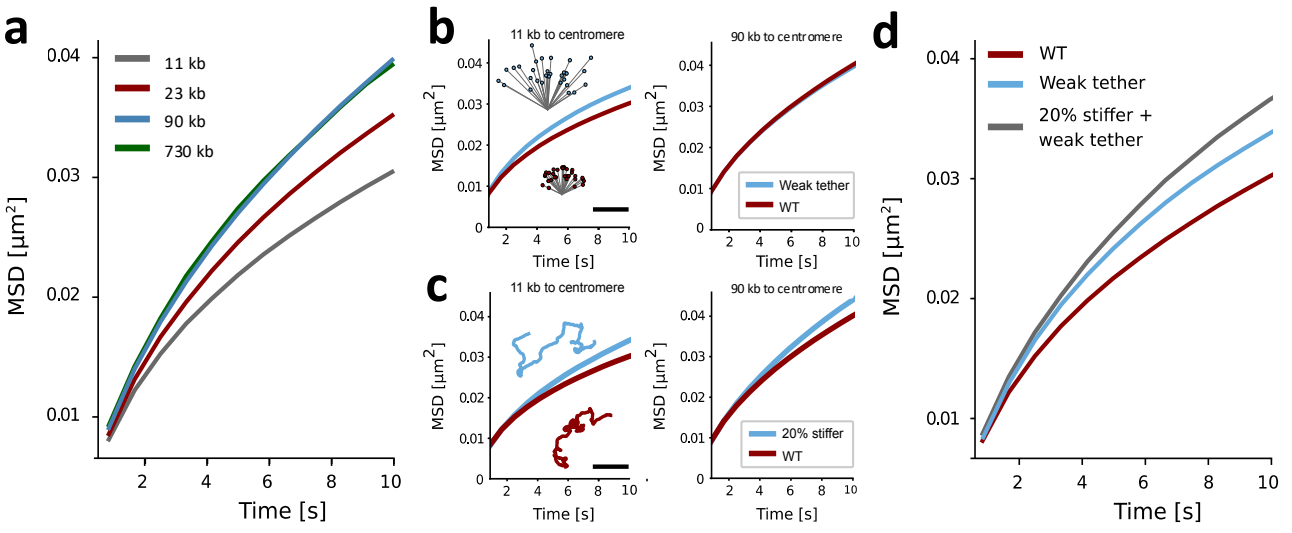
a
11 kb
23 kb
90 kb
730 kb
MSD [µm²]
Time [s]
b
11 kb to centromere
90 kb to centromere
Weak tether
WT
c
11 kb to centromere
90 kb to centromere
20% stiffer
WT
d
WT
Weak tether
20% stiffer +
weak tether

Fig. 5

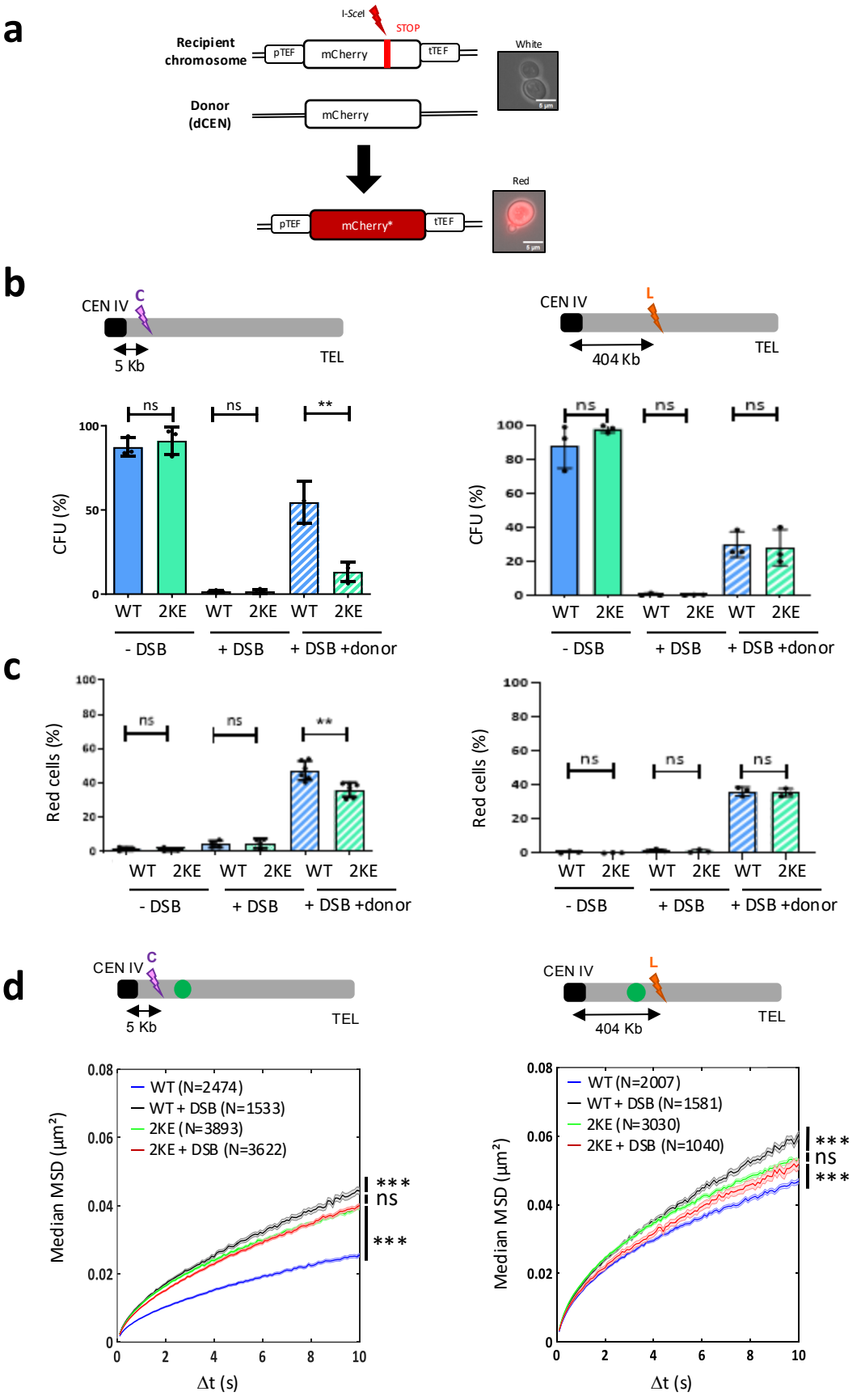
a
I-SceI
STOP
Recipient chromosome
pTEF
mCherry
tTEF
White
Donor (dCEN)
mCherry
Red
pTEF
mCherry*
tTEF
b
CEN IV
C
5 Kb
TEL
CEN IV
L
404 Kb
TEL
CFU (%)
ns
ns
**
ns
ns
ns
WT
2KE
- DSB
+ DSB
+ DSB +donor
c
Red cells (%)
ns
ns
**
ns
ns
ns
d
CEN IV
C
5 Kb
TEL
CEN IV
L
404 Kb
TEL
Median MSD (µm²)
WT (N=2474)
WT + DSB (N=1533)
2KE (N=3893)
2KE + DSB (N=3622)
***
ns
***
WT (N=2007)
WT + DSB (N=1581)
2KE (N=3030)
2KE + DSB (N=1040)
***
ns
***
Δt (s)

Fig. 6

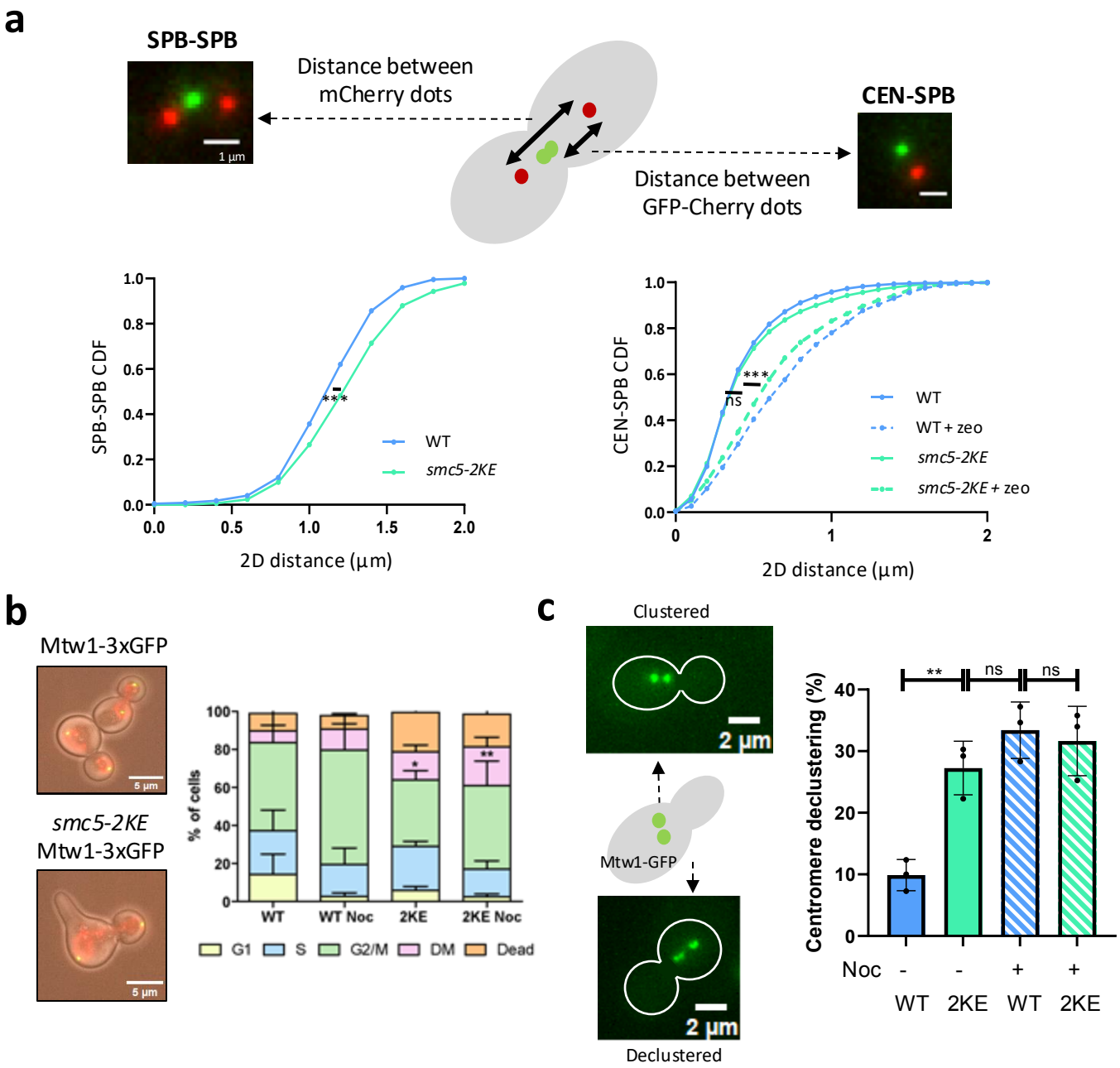
a
SPB-SPB
1 µm
Distance between mCherry dots
CEN-SPB
Distance between GFP-Cherry dots
SPB-SPB CDF
2D distance (µm)
***
WT
smc5-2KE
CEN-SPB CDF
ns
***
WT
WT + zeo
smc5-2KE
smc5-2KE + zeo
b
Mtw1-3xGFP
5 µm
smc5-2KE Mtw1-3xGFP
% of cells
WT
WT Noc
2KE
2KE Noc
G1
S
G2/M
DM
Dead
c
Clustered
2 µm
Mtw1-GFP
Declustered
Centromere declustering (%)
**
ns
ns
Noc
WT
2KE
WT
2KE